Additive Manufacturing 73 (2023) 103686



Contents lists available at ScienceDirect

Additive Manufacturing

journal homepage: www.elsevier.com/locate/addma

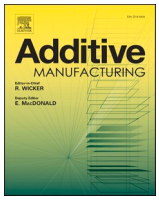



# Experimental and computational analysis of site-specific formation of phases in laser powder bed fusion 17–4 precipitate hardened stainless steel

Michael P. Haines [a], Maxwell S. Moyle [a], Vitor V. Rielli [a], Vladimir Luzin [b,c], Nima Haghdadi [a], Sophie Primig [a,*,1]

[a] School of Material Science and Engineering, UNSW Sydney, Sydney, NSW 2052, Australia
[b] Australian Nuclear Science and Technology Organisation (ANSTO), Sydney, Australia
[c] School of Engineering, The University of Newcastle, Callaghan, Australia

ARTICLE INFO

*Keywords:*
Additive manufacturing
17–4 PH stainless steel
Simulation
Solidification
Microstructure

ABSTRACT

Additive manufacturing allows for the production of intricate geometries with reduced material waste. However, due to the complex thermal gyrations that are linked to the processing parameters and geometry, inconsistencies in microstructures and mechanical properties occur from build to build. These inconsistencies are exemplified in multi-phase alloys such as 17–4 precipitation hardened (PH) stainless steel where the formation of ferrite, austenite, and martensite is sensitive to the powder composition and thermal conditions. The work presented here investigates a concentric scan strategy's impact on thermal conditions within laser powder bed fusion (PBF-LB/M) processed 17–4 PH stainless steel, and the resulting phase formation and morphologies that occur. Through the combined use of computational materials science and experimental characterization, complex phase transformation routes were identified as being dependent on the site-specific thermal gyrations within the builds. Within the outer regions of the builds, a primarily $\delta$-ferrite solidification microstructure was identified with two notable morphologies of austenite detected, allotriomorphic and Widmanstätten austenite. Within the center of the sample, however, a primarily austenite microstructure that nucleated from the prior $\delta$-ferrite was identified. Small fractions of $\alpha$-ferrite and/or martensite were potentially identified within the austenite grains. These results are rationalized using computational thermodynamics and kinetics in conjunction with proposals for pathways towards site-specific control of phase formation and morphology in PBF-LB/M stainless steels.

## 1. Introduction

The enthusiasm around metal additive manufacturing (AM) is due to its ability to produce highly complex geometries with less material waste that are not straightforward or impossible to be made via traditional subtractive manufacturing methods [1]. Despite the numerous advantages of AM, its adoption has not been immediate due to process variations that make it hard to produce consistent microstructures and mechanical properties [2–4]. Multi-phase (polymorphic) alloys are more sensitive to these process variations than single phase ones. 17–4 precipitation hardened (PH) stainless steel, for example, is particularly sensitive to process variations. Under traditional manufacturing methods, 17–4 PH is a martensitic precipitation hardened stainless steel after applying a standard heat treatment that has found use in the aerospace, chemical, and nuclear industries due to its combination of good ductility, high strength, and excellent corrosion resistance [5]. Under AM, the final microstructure has been shown to vary greatly depending on processing conditions, with microstructures ranging between $\delta$-ferrite, austenite, martensite, and combinations thereof [6].

The specific causes for the large variations in the reported microstructure in 17–4 PH are related to its composition and sensitivity to cooling rate due to process variations. For instance, Meredith et al. [7] tested several powders from different powder suppliers and observed resulting retained austenite that varied from 0 to 81 vol% in their builds. These differences were attributed to the powder composition. Sun et al. [8] showed variations in retained austenite from 13.1% to 30.5% that appeared to be dependent on the sample geometry and sample position on the build plate. In their study, the variation in retained austenite was due to the impact that sample geometry and position had on the thermal history. Moyle et al. [9] demonstrated the impact of processing

* Corresponding author.
*E-mail address:* s.primig@unsw.edu.au (S. Primig).
[1] ORCID 0000-0002-7682-5899

https://doi.org/10.1016/j.addma.2023.103686
Received 9 March 2023; Received in revised form 28 May 2023; Accepted 1 July 2023
Available online 3 July 2023
2214-8604/© 2023 The Author(s). Published by Elsevier B.V. This is an open access article under the CC BY-NC-ND license (http://creativecommons.org/licenses/by-nc-nd/4.0/).

parameters on the resulting retained austenite content based on changes in scan strategy. Similarly, they attributed differences in thermal history as the primary factor impacting austenite formation in their build.

The sensitivity of 17–4 PH to composition originates from certain elements stabilizing either the ferrite (Cr, Mo, Si, and Nb) or austenite (Ni, C, N, and Mn) phases [7]. Many studies often express the compositional sensitivity through the $Cr_{eq}/Ni_{eq}$ ratio. In general, the higher the $Cr_{eq}/Ni_{eq}$ ratio, the more likely the alloy is to form ferrite. As discussed previously, however, the thermal history also impacts final microstructure. Upon solidification, ferrite or austenite can nucleate in PBF-LB/M 17–4 PH due to solute segregation at extremely high solidification rates stabilizing the phase that forms at the higher temperature [10]. Within the literature, there have been multiple reports of 17–4 PH solidifying with either austenite or ferrite microstructures [6,11,12].

Similarly, the transformation of phases in the solid state is critically dependent on both composition and cooling rate. For instance, Vunnam et al. [6] showed a dependence on the transformation from $\delta$-ferrite to austenite and then to martensite to be dependent on the powder composition. The alloy with the higher $Cr_{eq}/Ni_{eq}$ of 2.76 showed a mostly $\delta$-ferrite microstructure with some martensite while the alloy with a $Cr_{eq}/Ni_{eq}$ of 2.43 showed a mostly martensitic microstructure. Both alloys showed small amounts of retained austenite. Alnajjar et al. [13] have described austenite by-passing within their PBF-LB/M 17–4 PH steel noting the impact of cooling rate. Due to the high cooling rates present in PBF-LB/M in combination with a composition that resulted in more sluggish austenite transformation kinetics, they reported that the formation of austenite from the $\delta$-ferrite was suppressed for their build.

The complexity of the phase transformation pathways in 17–4 PH due to sensitivity towards the cooling rate and initial powder composition are the primary causes for the large disparity in reported final as-built microstructure. The cooling rate is inherently linked to the detailed processing parameters including scan strategy and build geometry, whereas the powder composition and morphology is linked to the powder manufacturing route (e.g. the use of Ar versus $N_2$ as a cover gas in the gas atomization process [7]). These variations are detrimental to industry processes that rely on consistency and reproducibility. For instance, with increases in austenite, there is generally an increase in the toughness and ductility of the material with a decrease in the resulting yield and ultimate tensile strength. Further, the transformation induced plasticity (TRIP) effect has also been reported in some 17–4 PH builds due to transformation of austenite to martensite [14]. 17–4 PH builds with higher martensite and/or ferrite and lower austenite content are reported to have higher hardness and yield strength but lower ductility [8,15].

The work presented here builds on previous work by some of the current authors [9] where we demonstrated the impact of scan strategy on the final resulting microstructure. We showed a clear impact on the final fraction of austenite and ferrite, which was attributed to the impact of the scan strategy on the thermal history. The work presented here will, in greater depth, analyze the links between the thermal conditions and final phase in 17–4 PH through a combination of experimental characterization and the use of thermodynamic and kinetic models for the analysis of the evolution of phases in 17–4 PH. The motivation is to explain systematically how changes in the resulting thermal conditions due to complex scan strategies such as a concentric scan pattern may be used to achieve site-specific control of the microstructure.

## 2. Materials and methods

### 2.1. Experimental procedures

The composition of the gas atomized 17–4 PH powder, provided by 3D systems, is given in Table 1. The powder had a mean particle size of 11.8 μm. A more in-depth review of the powder characteristics on the same powder has been published elsewhere [9]. Builds were produced with cuboidal geometries with dimensions of 10 mm × 10 mm × 15 mm and were printed in an $N_2$ atmosphere using a 3D Systems ProX 300 PBF-LB/M machine. A concentric scan strategy, as outlined in Fig. 1, was used. The scan strategy follows a square path that starts at the perimeter of the build before moving inward, reversing course with each pass. The processing parameters utilized were the 3D system standard parameters which were a laser power of 127.5 W, scanning speed of 1200 mm/s, hatch spacing of 50 μm, layer height of 40 μm, and a laser diameter of 90 μm.

Samples were sectioned and then ground using SiC papers up to 4000 grit and polished to a mirror finish with 3 and 1 μm diamond suspensions. Following mechanical preparation, samples were eletro-polished using Struers A2 etchant for 20 s at 25 V. Some samples were also etched using Fry's reagent (40 mL HCl, 5 g $CuCl_2$, 30 mL water, 25 mL ethanol) for 5 s to reveal solidification microstructures. Micrographs were acquired on a JEOL 7001F scanning electron microscope (SEM) with an acceleration voltage of 15 kV and probe current of 8 nA. Electron backscatter diffraction (EBSD) was performed using a Hikari-EDAX camera mounted on the same SEM. EBSD data were captured using the following parameters: 20 kV acceleration voltage, 13 nA probe current, and 8 × 8 binning. The TSL OIM 8.0 software was used for EBSD data analysis.

Electron probe microanalysis (EPMA) was conducted on a JEOL JXA-8500F field emission SEM to analyze compositional differences across the samples. This SEM is equipped with a JEOL silicon drift detector energy dispersive spectrometer and wavelength dispersive spectrometers. The working distance was 10 mm, probe current was 500 nA, acceleration voltage was 15 kV, and a dwell time of 20 ms/pixel was used. The elements considered were Cr, Ni, Mn, Mo, Cu, Si, Nb, C, and N.

Site-specific atom probe tomography (APT) samples were prepared using a focus ion beam milling technique as described by Rielli et al. [16] on a ThermoFisher Helios G4 Xe PFIB. A straight flight CAMECA LEAP atom probe with 57% detector efficiency was used in laser-assisted mode to collect APT data. Parameters were as follows: 200 kHz pulse rate, 50 pJ laser energy, and 0.5% detection rate at a temperature of 50 K. Data analysis was performed using CAMECA AP Suite 6.1 software. For 1D concentration profiles, analyses were done along the z direction of a 20 × 20 × 40 $nm^3$ cylinder across the interphase boundary with a bin width of 0.5 nm. Bulk compositions for ferrite and

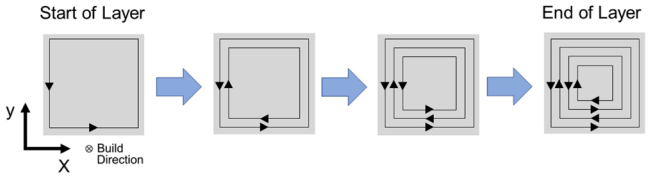


**Fig. 1.** Schematic of the concentric scan strategy used in the build. The laser starts at the perimeter of the build and moves inwards on each pass. The build direction is facing into the page as indicated.

**Table 1**
Composition of 17–4 PH stainless steel powder measured from inductively coupled plasma atomic emission spectrometry (ICP-AES).

| Element | Fe | Cr | Ni | Cu | Mn | Si | Nb | Mo | N | C |
|---|---|---|---|---|---|---|---|---|---|---|
| **Concentration (wt%)** | Bal. | 16.1 | 4.34 | 3.81 | 0.87 | 0.71 | 0.32 | 0.13 | 0.1 | 0.03 |
| **Concentration (at%)** | Bal. | 17.04 | 4.06 | 3.30 | 0.87 | 1.39 | 0.19 | 0.07 | 0.39 | 0.14 |

austenite were obtained within a 30 × 30 × 80 $nm^3$ cylindrical regions of interest positioned on the center of each phase in the APT dataset.

An Alemnis nanoindenter was used that was installed in a FEI NOVA NanoSEM 230 with a conductive-diamond cube corner indenter tip. Nanoindentation tests were performed under load control with a target load of 20 mN and 5 s holding at maximum load, corresponding to indentation depth of 1 – 1.2 μm. Indents were performed in a row across the center of the sample with a spacing of 15 μm. Direction observation of the tip apex and local microstructure was allowed through in-situ measurements with the cube corner probe. Tip area calibration was performed in fused silica.

Neutron diffraction experiments for collecting three-dimensional residual stress data were carried out at Australia's Nuclear Science and Technology Organisation (ANSTO) to underpin the discussion of results. The experimental details and results are available in the Supplementary File (Section S1).

### 2.2. Numerical simulations

To better understand the phase transformation pathways in 17–4 PH builds, knowledge of both the thermal history and the solidification conditions at the melt pool is essential. To predict these thermal histories and solidification conditions, a code developed by Oak Ridge National Lab for use in OpenFOAM was utilized. A short description of the numerical procedures are given here; however, a more detailed description can be found in [17].

The governing equation for the thermal simulation only accounts for conduction in the material, energy input from the laser, and evolution of latent heat from individual phases. The role of fluid flow on the melt pool was ignored due to its large impact on computation time while not appreciably impacting solidification parameters such as the thermal gradients and solidification velocity [17,18]. The governing equation is, thus, given as

$$\frac{\partial(\rho c_p T)}{\partial t} = \nabla \bullet (k \nabla T) + S_T + \dot{Q}$$

where $S_T$ is the energy source term that accounts for the evolution of latent heat during phase change, $T$ is the temperature, $k$ is the coefficient of conduction, $t$ is the time, $c_p$ is the mixture specific heat, and $\rho$ is the mixture density. $\dot{Q}$ is the volumetric energy term and utilizes the Gaussian heat source proposed by Goldak et al. [19] and is described as

$$\dot{Q}(x,y,z) = \frac{2\eta P}{r^2 d \left(\frac{\pi}{3}\right)^{\frac{3}{2}}} \exp\left( -\frac{3(x^2+y^2)}{r^2} + \frac{-3z^2}{d^2} \right)$$

where $d$ is the penetration depth, $r$ is the radius of the laser, $\eta$ is the laser absorption efficiency, and $P$ is the laser power. A subsection of the build geometry was modeled due to computational limitations. Therefore, the geometry modeled was a cuboid of 10 mm × 10 mm × 1.5 mm. The mesh was discretized into 1.5 million elements with intent to capture the rough shape of the solidification boundary of the melt pool. The sides and bottom of the geometry had adiabatic boundary conditions. The top of the geometry had a convection and radiation boundary condition given as

$$q_c = h_c(T - T_a)$$

$$q_r = \varepsilon\sigma\left(T^4 - T_a^4\right)$$

where $q_c$ is the heat flux from convection, $h_c$ is the coefficient of convection, $T_a$ is the temperature of the atmosphere, $q_r$ is the heat flux due to radiation, $\varepsilon$ is the emissivity, and $\sigma$ is the Stefan-Boltzmann constant ($5.67 \times 10^{-8}$ W/$m^2$). The material properties for specific heat and conduction utilized separate polynomial equations for the liquid and the solid and are given in Table 2. These parameters were obtained from [20]. Latent heat of fusion, liquidus temperature and solidus temperature, given in Table 3, were calculated from ThermoCalc. Penetration depth ($\sigma_z$) and laser efficiency ($\eta$) were used as calibration parameters such that the melt pool width and depth in the simulation was matched to the physical melt pool dimensions observed from etched micrographs. Overlays of the simulated melt pool on the etched micrograph can be found in the supplementary file (Fig. S2). All other material properties and their associated reference, if applicable, are provided in Table 3.

**Table 2**
Polynomials used for material properties in the OpenFOAM thermal analysis.

| Property | Polynomial | Units |
|---|---|---|
| **Solid** | | |
| Specific heat, $c_p$ | $509.09 + 0.168T$ | J ($kg^{-1}$ $K^{-1}$) |
| Thermal conductivity, $k$ | $2.172 + 0.025T + 4.71 \times 10^{-6}T^2$ | J ($m$ $s^{-1}$ $K^{-1}$) |
| **Liquid** | | |
| Specific heat, $c_p$ | $693.72 + 0.0743T$ | J ($kg^{-1}$ $K^{-1}$) |
| Thermal conductivity, $k$ | $62.23 - 0.0496T + 1.64 \times 10^{-5}T^2$ | J ($m$ $s^{-1}$ $K^{-1}$) |

An interface response function (IRF) model was used to outline the impact that thermal gradients (G) and solidification velocities ($V_s$) can have on the phase formation and morphology. These models are able to make predictions on microstructure based on the stability of the solid-liquid interface. The model used here was initially developed by Kurz, Giovanola, and Trivedi and is known as the KGT model [23]. Fukumoto and Kurz [24] used the KGT model to develop phase and microstructure maps for a Fe-Cr-Ni alloy based on the solidification velocity in directional solidification and laser experiments. For our model, material properties were taken from ThermoCalc using the TCFE11 database and thermal gradients and solidification velocities were taken from the aforementioned OpenFOAM thermal simulation to create the resulting phase maps. Details on the implementation can be found in the following references [10,25] and in the Supplementary File (Section S3).

## 3. Results

### 3.1. Crystallography and phase

The concentric scanning strategy used for the production of the builds has the laser beam travel from the outer edge of the geometry inwards in repeating smaller square paths. The resulting path causes the inner region to experience a greater heat input over a shorter period of time compared to the outer region. The impact of the concentric scan strategy on the resulting microstructure can be clearly seen in the EBSD results in Fig. 2 shown for the center XY plane of the sample. Fig. 2a shows the inverse pole figure (IPF) map giving a clear distinction between a coarse grain region towards the edge of the map and a fine grain region towards the center of the map before returning to a smaller coarse grain region at the exact center. Further, within the outer region of the

**Table 3**
Material properties used in the OpenFOAM thermal analysis.

| Properties | Values | Units | Ref. |
|---|---|---|---|
| Liquidus temperature, $T_{liq}$ | 1711 | K | |
| Solidus temperature, $T_{sol}$ | 1659 | K | |
| Atmospheric temperature, $T_a$ | 300 | K | |
| Latent heat of fusion, $L_f$ | $2.9 \times 10^5$ | J $kg^{-1}$ | |
| Latent heat of vaporization, $L_v$ | $6.1 \times 10^6$ | J $kg^{-1}$ | [18] |
| Evaporation temperature, $T_v$ | 2930 | K | |
| Molecular mass, $M$ | 0.0061 | kg $mol^{-1}$ | [18] |
| Emissivity, $\varepsilon$ | 0.35 | | [21] |
| Convection coefficient, $h_c$ | 10 | W $m^{-2}$ K | [22] |
| Beam diameter, $\sigma_{xy}$ | $90.0 \times 10^{-6}$ | m | |
| Penetration depth, $\sigma_z$ | $100.0 \times 10^{-6}$ | m | |
| Laser efficiency, $\eta$ | 0.75 | | |

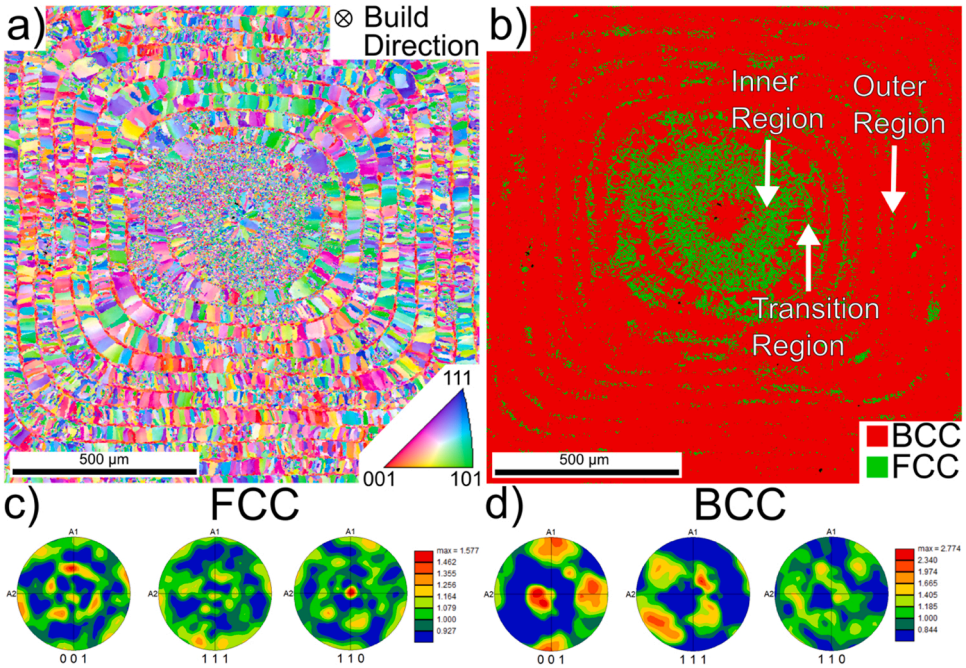


**Fig. 2.** EBSD analysis of the center of the build in the XY plane with build direction pointed into the page. a) IPF map, b) phase map, c) pole figure of the FCC grains d) pole figures of the BCC grains. Pole figures were calculated from an EBSD dataset shown in Supplementary Fig. S3.

sample a clear bimodal grain size is observed. Circular patterns of smaller banded grains with a strong < 100 > direction (red) parallel to the build direction (<100 > // BD) are surrounded by larger grains of more random orientations. The solidification of the melt pool is responsible for this grain microstructure with the smaller < 100 > grains forming at the center of the melt pool [26]. The thermal gradients at the solid-liquid interface of the melt pool is likely highest in this region due to the majority of the thermal conduction facing predominantly down the build, parallel yet opposite of the build direction [27]. The phase map presented in Fig. 2b shows that the coarser grain regions are mostly body centered cubic (BCC) while the fine grain regions are mostly face centered cubic (FCC). A smaller phase map of the same sample was shown in our previous work [9], however, the focus was on the texture evolution in those samples. Three regions are identified and marked with arrows in this phase map: An outer region, consisting mostly of BCC; a transition region, where a larger fraction of FCC has started to form; and an inner region, consisting mostly of FCC. Using a secondary EBSD dataset presented in the Supplementary File as Fig. S3, pole figures of the grain orientation are given in Fig. 2c and d for the BCC and FCC phases, respectively. The pole figures reveal that the BCC grains have a slight tilt away from the < 100 > // BD. The FCC grains exhibit a weaker texture in the < 110 > direction. In comparison to the BCC phase, the FCC shows a more random texture, which could be an indication that these grains nucleated from the BCC grains and were not influenced by the melt pool and, thus, local solidification conditions. Overall, the BCC shows a maximum texture index of 2.8 multiples of randomness while the FCC shows a maximum texture index of 1.6 multiples of randomness.

### 3.2. Austenite and ferrite phase morphology

Higher resolution EBSD in the XY plane was collected in the outer ferritic region (Fig. 3a-b), the transition region where the phase fractions change from predominately BCC to FCC (Fig. 3c-d), and in the center FCC region (Fig. 3e-f), to reveal more detailed information on the morphology and structure of the FCC and BCC phases. The black arrows in Fig. 3a,c point into the direction of travel of the melt pool. In the outer regions of the sample, appearing along BCC grain boundaries, two distinct morphologies of FCC are present, allotriomorphic and Widmanstätten austenite. The allotriomorphic austenite, labeled in Fig. 3a as $\gamma_a$, is present in the center of the EBSD as small grains that decorate the BCC grain boundaries. Their formation strongly aligns to regions of smaller BCC grains with higher grain boundary density, with the largest number appearing towards regions coinciding with the center of melt pool tracks. Further, some of these grains are noted as having twins (highlighted in yellow in Fig. 3a,b), likely due to high amounts of residual stress that are inherent to the PBF-LB/M process [28]. Widmanstätten austenite, labeled in Fig. 3b as $\gamma_w$, was noticed at the grain boundaries towards the bottom right of the EBSD map. A single, elongated austenite grain is noted to form between two BCC grains. Branching laths growing from this single austenite grain indicates that this long grain is of Widmanstätten morphology. These grains appear to mostly form perpendicular to the scan path direction along larger BCC grains.

Within the transition region (Fig. 3c-d), Widmanstätten and allotriomorphic austenite are similarly present, however, the associated features are larger compared to the austenite in the primarily BCC region. Similarly, a larger number of allotriomorphic austenite has formed along the center of the melt pool track and along larger BCC grains, while Widmanstätten austenite has only formed perpendicular to the melt pool's direction of travel. In the EBSD taken in the inner austenite region (Fig. 3e-f), the different morphologies of austenite have become more difficult to distinguish due to the growth of austenite from the repeated thermal gyration from the scan strategy. Overall, a larger number of striated austenite and interwoven BCC structures are noted. Similarly, twinning could be identified in some of the austenite grains. Some BCC was also noted within the austenite grains. These BCC grains could be either martensite, the prior solidified microstructure, or new, precipitated BCC grains. The difference between martensite and ferrite cannot be explicitly made here due to EBSD not being able to distinguish these two phases due to the low carbon content of the sample resulting in both being identified as BCC [29].

To better understand the origin of the BCC and austenite phases as identified by EBSD in the center of the sample, etching with Fry's reagent was performed. The chemical variation upon solidification is expected to result in preferential etching of the interdendritic regions of

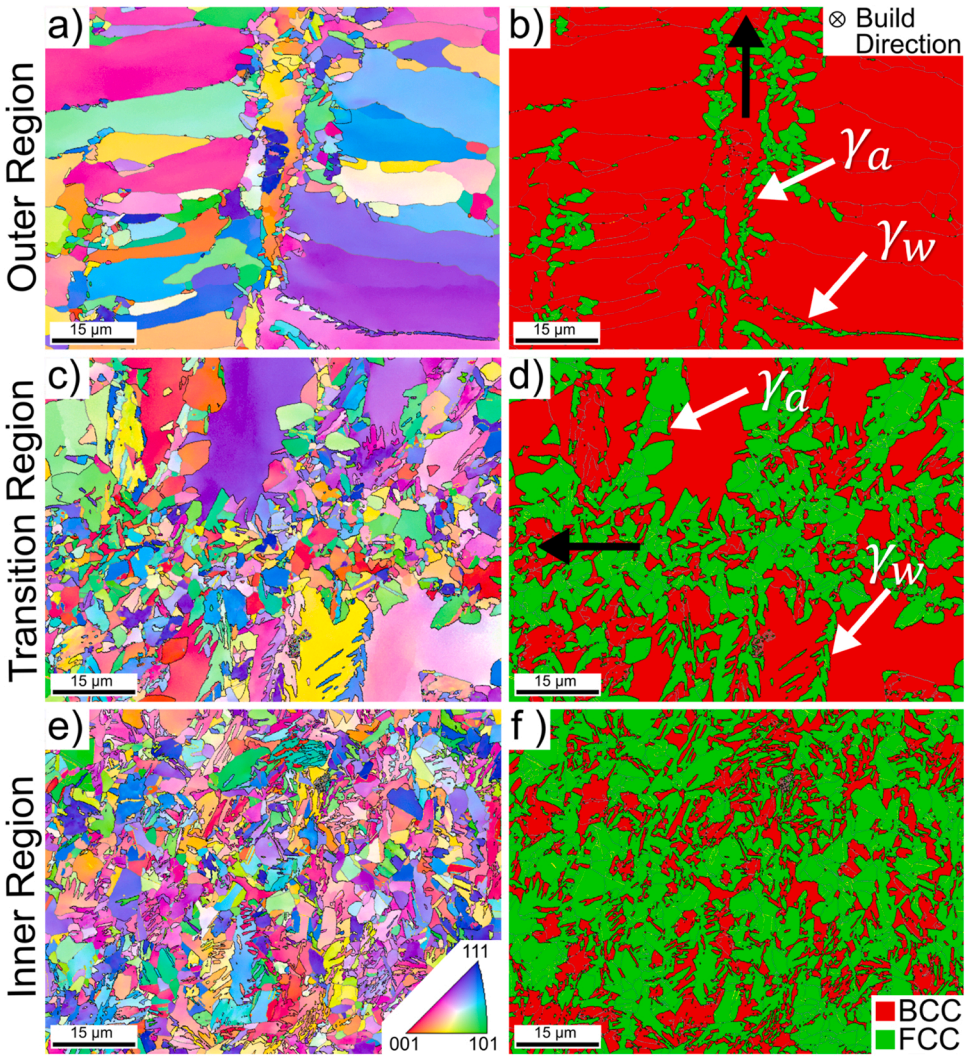


**Fig. 3.** EBSD analysis of FCC and BCC grains in the XY plane with build direction facing into the page. (a, c, e) IPF maps, and (b, d, f) phase maps. (a,b) were taken in the outer BCC region of the sample, (c, d) were taken in the transition zone between the outer BCC region and inner austenitic region, and (e, f) were taken in the inner austenitic region. Black lines represent boundaries between phases and gray lines represent boundaries between grains. Yellow lines show twinning in the Austenite. The black arrows point in the direction of the scan path.

the sample compared to the dendritic regions. Therefore, the etching will allow identification of rough dendritic microstructures as solidification structures, while smoother regions can be identified as coming from solid-state transformations [30,31]. SEM micrographs and EBSD were conducted to identify these different regions. Fig. 4a shows an XY plane micrograph that had its perspective corrected from the 70° sample tilt to match the accompanying EBSD maps for better comparison of features. IPF and phase maps combined with image quality (IQ) are given in Fig. 4b-c. Based on the phase map (Fig. 4c), the rough microstructures with a dendritic BCC structure show solidification as $\delta$-ferrite. The smooth regions within the etched micrograph, however, correlate primarily to grains of austenite with some internal BCC structures (Fig. 4b-c). Here, a solid-state transformation from $\delta$-ferrite to austenite would have likely occurred due to the lack of dendrites present, while the internal BCC structures transformed from the austenite through yet another solid-state phase transformation from austenite to ferrite.

The solid-state transformed ferrite has mostly formed as individual bands within the austenite grains, however, some notable features pointed at by white arrows in Fig. 4b-c show some grains with collections of BCC lath structures. While these could be martensite, as mentioned previously, it is not possible to differentiate the ferrite from martensite, thus, confirmation on the formation of martensite cannot be made here. Further, if these are martensite phase structures it should also be noted that they were not likely induced through the polishing routines used as the samples presented here were electropolished.

### 3.3. Chemical heterogeneities

An EPMA map taken from the XY plane center left of the sample with a dimension of 445 μm × 202 μm is presented in Fig. 5. The scan region here was specifically chosen to capture both the predominantly austenite region and predominately ferritic outer regions. With the exception of a few elements such as Mn, Si, O, and C, no major compositional partitioning can be seen locally or between the primarily ferrite and austenite regions. Of note, however, these results do not necessarily point towards the occurrence of solute trapping as often the microsegregation in PBF-LB/M is in the nanoscale below the excitation volume of EPMA [32]. These results, however, indicate a lack of long-range diffusion that could come from elevated build temperatures and will help in determining the transformation mechanism of austenite. Looking at the few elements that show segregation, Mn is noted to partition in certain regions including around those outer regions of the austenite at the center of the sample, however, it is noted that the Mn returned to similar levels after quickly moving away from the edge of the FCC center. (Si, Mn) oxides and/or carbides are also noted to form, and this has also been reported in several other studies on stainless steels printed by PBF-LB/M [29,33]. EPMA data was also collected for Cr, N, and Mo, however, these maps present no compositional variations and, therefore, were not included here for brevity. A second EPMA dataset was collected for the outer region of the sample showing the same trend as presented in Fig. 5. These extra maps are included as Supplementary

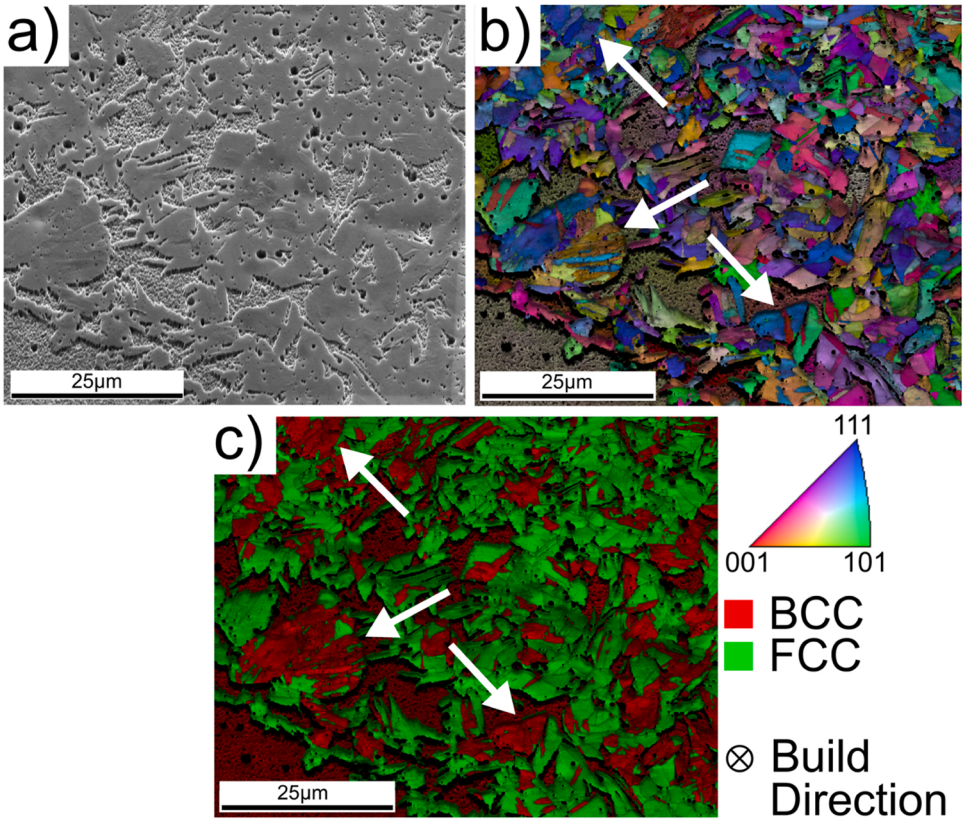


**Fig. 4.** Micrographs of an etched surface: SEM (a) and EBSD analysis (b, c) of the inner austenite region in the XY plane with the build direction facing into the page. (b) is IPF + IQ and (C) is phase + IQ. The rough regions in the images are dendritic structures while the smoother regions represent phases that have undergone a solid-state transformation. White arrows point towards larger collections of BCC grains that have the possibility of being martensite, but could not be identified further through EBSD techniques used here.

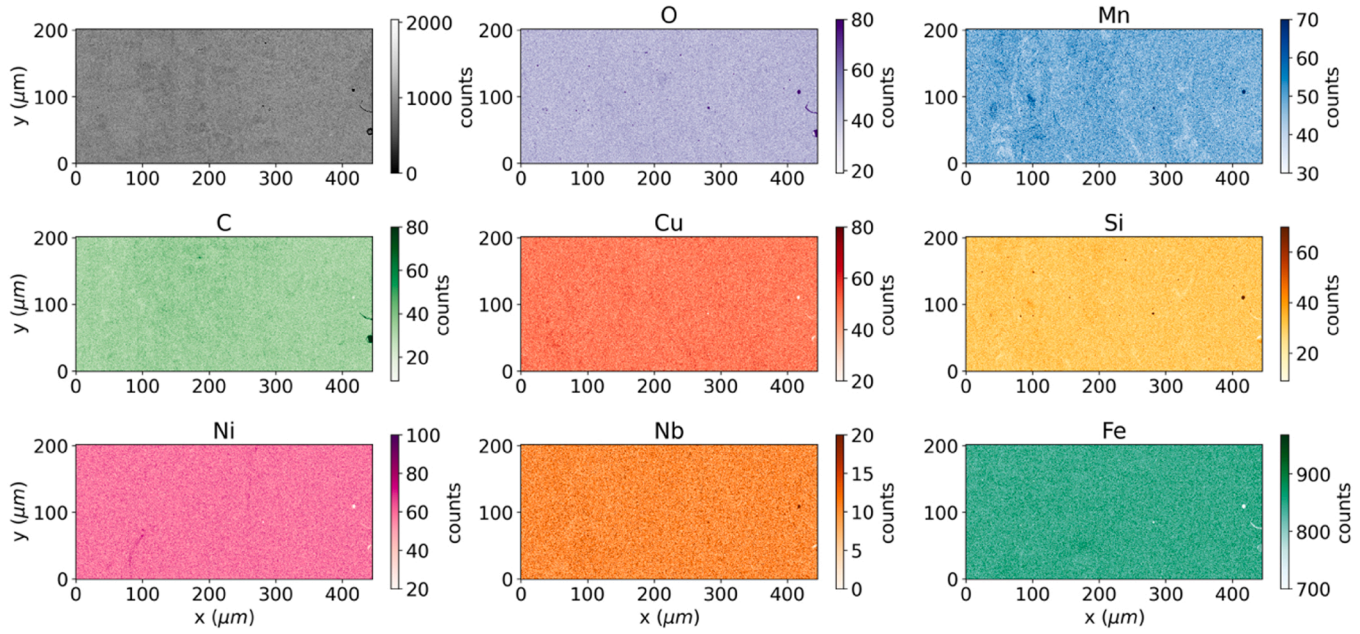


**Fig. 5.** EPMA of the center left region of the sample for the XY plane, with the center of the sample being at the right edge. The build direction faces into the page.

Fig. S4.

To advance understanding of the differences between the austenite and ferrite, site-specific APT was performed to analyze a ferrite/austenite interface towards the center of the sample, as presented in Fig. 6. The tip was extracted roughly 80 μm offset from the center of the build, parallel to the XY plane, such that it was extracted from the predominantly austenite region. A grain boundary is clearly visible in the center of the tip. The identities of the phases on either side of the grain boundary can be potentially confirmed through investigation of the formation of Cu precipitates. Due to higher rates of diffusion of Cu in ferrite when compared to austenite as has been reported in literature [14,34], austenite is likely to see noticeably different Cu clustering and precipitation compared to ferrite. Fig. 6a presents a reconstruction, using a Cu isovalue commonly used in the literature of 10 at% [35–37], which reveals a clear distinction between the top and bottom grains, with the latter having Cu precipitates with an average diameter of 2.5

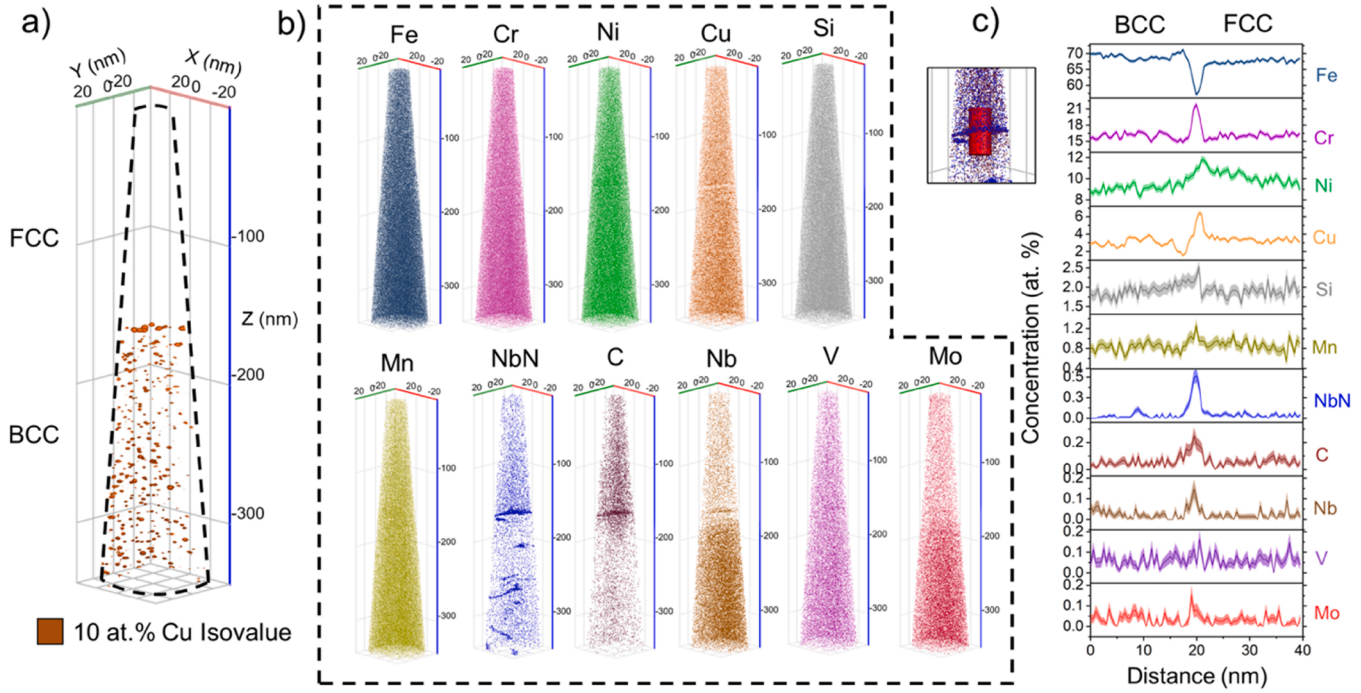


**Fig. 6.** (a) Precipitates observed in ferrite with a Cu isovalue of 10 at%. (b) Atom maps of the tip containing austenite (top) and ferrite (bottom). (c) 1D composition profile of the red cylinder (inset) along the interphase boundary. Filled areas show 2σ errors in (c).

± 1.4 nm. Precipitates on the grain boundary are larger with a diameter of 4.3 ± 1.3 nm. Therefore, the bottom grain can be identified as ferrite due to the large number of precipitates, while the upper grain can be identified as austenite.

Inspection of the atom maps in Fig. 6b reveals visual evidence of segregation in C, Nb, Mo, and NbN which contrasts with the EPMA results that show no differences between austenite and ferrite on the μm scale. Further, C and NbN are noted to segregate to the austenite/ferrite interface. NbN is also seen segregating to what are likely dislocations in the ferrite. It should be noted that due to overlap between the Si and N spectrum peaks, the NbN species was used to correlate the partitioning of N. The NbN atom maps align with the expected partitioning of N towards grain boundaries and dislocations. Discussion of N within this work will henceforth refer to the NbN species.

1D concentration plots across the interphase boundary are given in Fig. 6c and reveal increases in concentration for all elements at the interface, with the exceptions of V and Fe. V exhibits no change at the interface, while Fe sees a 10 at% depletion. Table 4 shows the bulk composition of ferrite and austenite extracted from the APT dataset. Broadly speaking, there is notable partitioning of solute content into the austenite phase, with significant increases in C and NbN, and slight increases in Cr, Ni, Cu, and Si compared to the bulk concentration of the ferrite phase. The ferrite phase has higher concentrations of Fe, Mo, and Nb. Overall, the amount of partitioning of elements in the bulk between these two phases is minor with most elements seeing < 5% difference in concentration with the exception of Mo, Nb, C, and NbN. Further the partitioning of Cr and Si to the austenite phase is interesting due to these elements traditionally being ferrite stabilizers.

### 3.4. Nanoindentation

Hardness results from nanoindentation are presented in Fig. 7. The EBSD phase map in Fig. 7a shows the representative region where the indents were carried out. The plot in Fig. 7b shows the phase fraction of δ-ferrite, calculated from the EBSD subsection presented in Fig. 7a, and

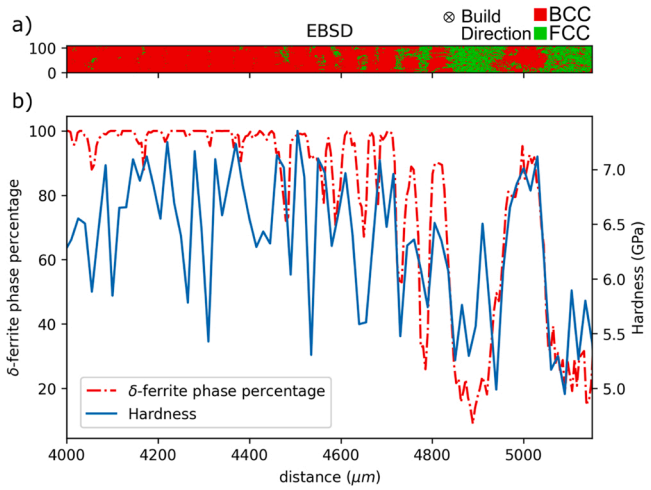


**Fig. 7.** a) EBSD phase map of the represented area where the hardness data was collected, b) Phase fraction of δ-ferrite (left), calculated from the EBSD phase map in a) and Hardness from nanoindentation (right).

**Table 4**
Bulk composition (at%) of austenite and ferrite measured by APT.

| | Fe | Cr | Ni | Cu | Si | Mn | NbN | C | Nb | V | Mo | P |
|---|---|---|---|---|---|---|---|---|---|---|---|---|
| FCC Austenite (Top) | 68.71 | 16.27 | 8.85 | 3.27 | 1.88 | 0.81 | 0.03 | 0.05 | 0.02 | 0.06 | 0.03 | 0.02 |
| | ±0.01 | - | - | - | - | - | - | - | - | - | - | - |
| BCC Ferrite (Bottom) | 69.49 | 15.79 | 8.69 | 3.15 | 1.81 | 0.80 | 0.01 | 0.01 | 0.08 | 0.06 | 0.07 | 0.04 |
| | ±0.06 | ±0.03 | ±0.02 | ±0.01 | ±0.01 | ±0.01 | - | - | - | - | - | - |

the hardness obtained from nanoindentation. Results going from the outer region of the sample towards the center show a fluctuation in the hardness as it indents regions of the harder ferrite and small pockets of the softer austenite. The hardness shows a consistent drop once reaching the primarily austenite region before reaching the ferrite in the center of the sample where hardness values increase to similar values as those seen in the outer region.

### 3.5. Thermal simulations

The thermal conditions play a significant role in impacting the resulting microstructure and phase evolution within PBF-LB/M printed materials. The thermal simulation results presented here give estimates on the cooling rate and potential thermal gyrations that may impact the microstructure based on input from the given concentric scan strategy and processing parameters. Fig. 8 shows the results from the thermal simulation at various time steps. A video of the thermal simulation is provided as Supplementary Video V1. At 0.002 s the melt pool shows a length and width of 0.269 mm and 0.082 mm, respectively, with a depth of 48 μm. By 1.62 s the length and width of the melt pool increases to 0.367 mm and 0.106 mm with a depth of 56 μm. By 1.6885 s, an area melt pool forms due to the quick circular motion of the laser beam and exists at the center of the part until 1.6915 s. Unlike a traditional line melt pool that follows the movement of the laser, this area melt pool is mostly static, maintained by the small circular movements of the laser at the center of the part. This melt pool had a length and width of roughly 0.40 mm and a depth of 112 μm at 1.6885 s. Overall, the increase in melt pool size from the edge of the sample to the center of the sample can likely be associated with the decrease in return time of the laser to a given area as the beam circles towards the center of the sample. The decrease in return time as the laser moves towards the center of the build would result in a reduced amount of time for a given area to cool.

As the G and $V_s$ are known to control the microstructure evolution in steels, G and $V_s$ across the XZ plane of the sample were extracted as shown in Fig. 9. Small variations in the G and $V_s$ can be seen moving from the edge towards the center of the sample. These variations in the G and $V_s$ clearly outline the individual melt pools. However, about 4.8 mm towards the center, a clear change occurs where the $V_s$ suddenly decreases. The decrease in $V_s$ correlates to the formation of the area melt pool around 1.6885 s as seen in Fig. 8, due to the consistent circling of the laser, resulting in a large amount of energy being inputted into a small area of the sample. This area melt pool is sustained for a short amount of time as the scan continues towards the center of the sample. Afterwards, during the melt pool's solidification, G will continue to decrease from the initial value at roughly 4.8 mm while $V_s$ increases due to the lack of energy input resulting in an increasing rate of solidification. Of note is that this initial high G and low $V_s$ pattern, from the solidification of the center area melt pool, that decreases and increases respectively as the melt pool further solidifies, is similar to the solidification seen with the spot melt scan strategy seen in PBF-EB processes [38].

### 3.6. Equilibrium phase calculations

A stepped equilibrium phase calculation was performed using ThermoCalc (Fig. 10) that shows the phase evolution and transformation temperatures under equilibrium conditions. Results show that from the liquid, $\delta$-ferrite forms at 1711 K. Austenite soon follows and forms at 1659 K. Austenite quickly becomes the dominant phase, and by 1605 K the $\delta$-ferrite has reached a phase fraction of 0. $\alpha$-ferrite precipitates at a temperature of 1038 K and soon becomes the dominant phase. These results therefore show the following solidification sequence:

$L \rightarrow L + \delta \rightarrow L + \delta + \gamma; \delta \rightarrow \gamma$ below the solidus

Other phases noted to appear are carbide and nitride phases starting at 1659 K. Lastly, a copper rich phase was noted to appear at 1259 K. At room temperature the predicted phase fractions are 7% austenite, 88% ferrite, and 5% other phases. It should be noted that the permitted compositional variations within 17–4 PH stainless steel allows for notable variations in the reported equilibrium phases. For instance, the calculations reported by Vunnam et al. [6] compared to the work reported here show nearly a 100 K difference in solidus and no stable austenite below 600 K despite both using the TCFE database developed by ThermoCalc.

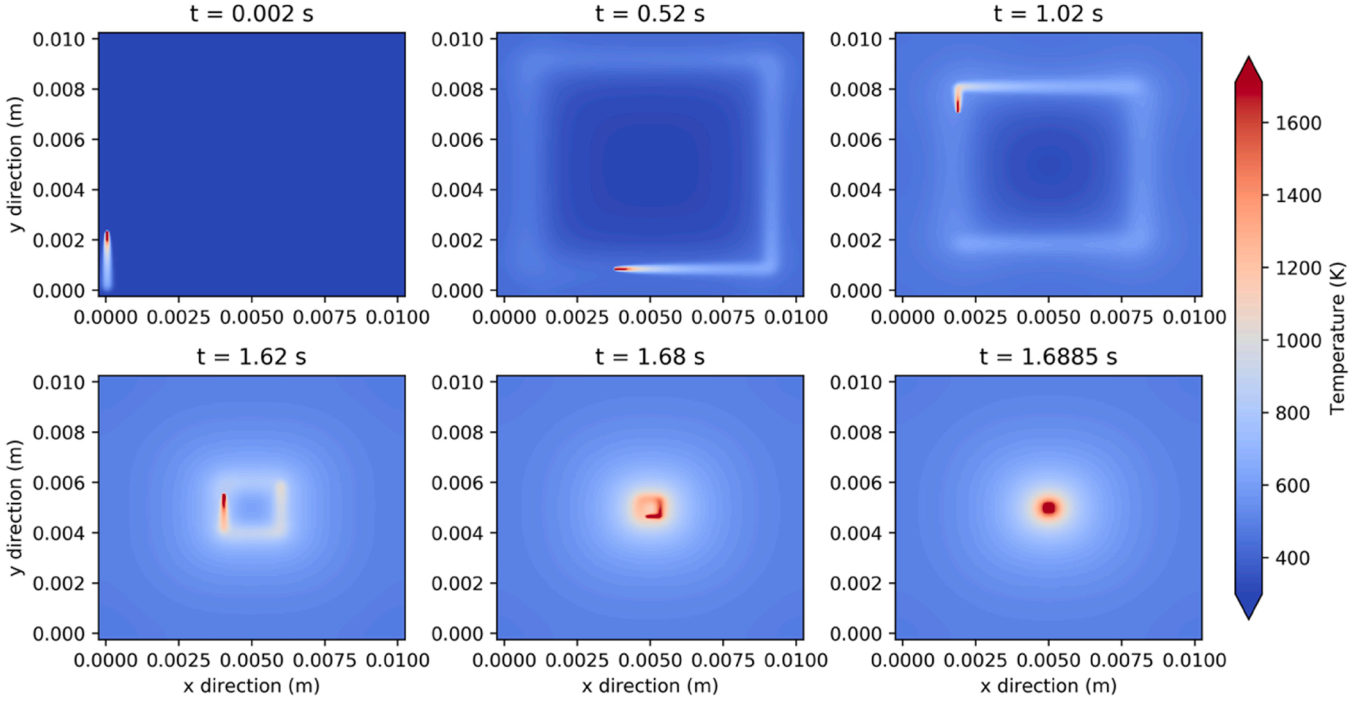


**Fig. 8.** Temperature maps of the XY plane obtained by the OpenFOAM heat transfer simulation showing the evolution of the melt pool over time.

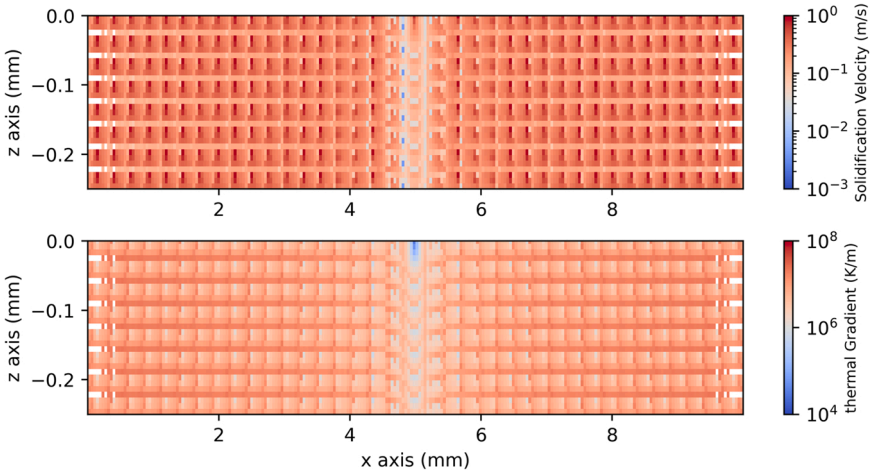


**Fig. 9.** Plots of the solidification velocity (Top) and thermal gradient (Bottom) for the XZ plane at the center of the sample.

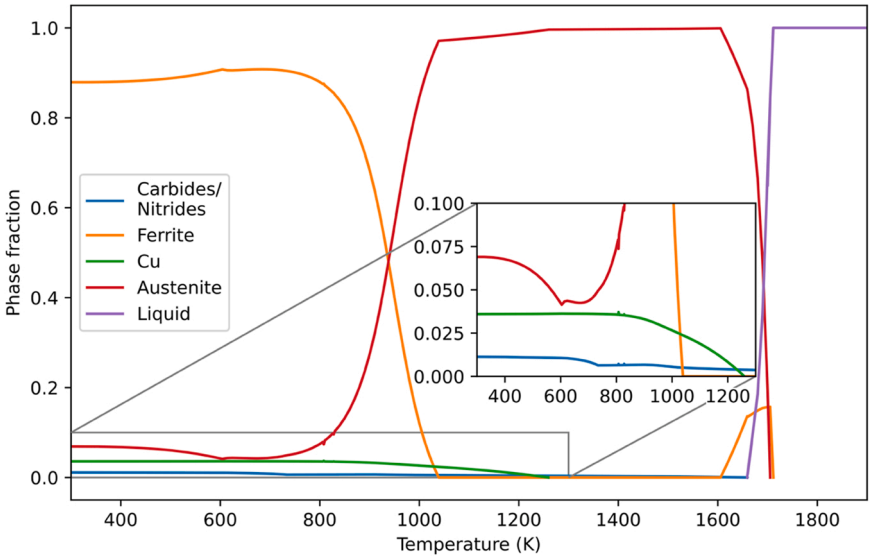


**Fig. 10.** Phase fraction versus temperature of 17–4 PH steel calculated from ThermoCalc.

## 4. Discussion

Prior literature has demonstrated that AM exhibits distinctive thermal conditions compared to other traditional manufacturing routes [39,40]. With the unique concentric scan strategy's clear impact on the resulting microstructure in 17–4 PH, it is important to consider how these changes in microstructure are correlated to changes in the solidification conditions and/or changing resulting thermal gyrations in the solid.

The different modes of solidification possible for stainless steels can range from austenite mode, ferrite mode or austenite + ferrite mode, and will be dependent on the composition and the G and $V_s$ [41,42]. After solidification, the microstructure has the opportunity to transform into ferrite, austenite, or martensite. This depends on the aforementioned solidification mode which will then influence subsequent solid-state transformation through both compositional partitioning at the time of solidification and local thermal gyrations that are dependent on the geometry, processing parameters, and scanning strategy.

### 4.1. Solidification microstructure

For PBF-LB/M 17–4 PH stainless steel, due to permitted compositional variations within the alloy specification, the solidification mode reported in literature has varied from austenite [11,43–45] to $\delta$-ferrite [6,8,9,45]. The impact of the composition has traditionally been explained through the $Cr_{eq}/Ni_{eq}$ ratio which takes into consideration ferrite and austenite stabilizing elements and is given as [45]:

$$Cr_{eq}\ (wt\%) = Cr + 2(Si) + 1.5(Mo) + 5(V) + 5.5(Al) + 1.75(Nb) + 1.5(Ti) + 0.75(W)$$

$$Ni_{eq}\ (wt\%) = Ni + (Co) + 0.5(Mn) + 0.3(Cu) + 25(N) + 30(C)$$

As the transition from austenite to ferrite solidification mode is dependent on the solidification condition, an exact $Cr_{eq}/Ni_{eq}$ ratio cannot be given. For example, under pulsed laser welding, the reported switch from austenite to ferrite mode occurred between a ~1.6 and ~1.7 $Cr_{eq}/Ni_{eq}$ ratio [46]. Under electron beam welding, it has been reported to be between 1.6 and 1.84 [41]. For PBF-LB/M, this switch is likely between 1.75 and 2.04 [8,45]. The alloy used in this work has a calculated $Cr_{eq}/Ni_{eq}$ ratio of 1.96. From the etched microstructure in Fig. 4, there is a strong correlation, with the rough dendritic regions correlating to BCC, pointing towards the primary solidification mode in the build being $\delta$-ferrite. This contradicts the thermodynamic equilibrium reported in Fig. 10 that showed a mixture of ferrite and austenite.

While there were drastic changes in the solidification conditions as evident in the G and $V_s$ plots in Fig. 9, these changes in solidification were not sufficient to change the primary solidification mode of this alloy based on identified solidification structures. Only primary $\delta$-ferrite solidification structures could be identified throughout the sample.

The presence of an austenite solidification mode can further be confirmed by an examination of the orientation of grains within the sample. The ferrite grains, being primarily solidification structures, show a stronger $< 100 >$ // BD texture within the pole figures in Fig. 2c. Often solidified grains in the PBF-LB/M process favor growth of the $< 100 >$ // BD. This texture results due to solidification of previous layers and the strong thermal gradients that point upwards towards the build direction [47]. The FCC grains, however, show an almost random texture in the pole figures presented in Fig. 2d, pointing towards these grains likely nucleating from a solid-state transformation that is influenced through grain boundary orientation relationships [13,48].

A last point of consideration pertaining to the changing of solidification phase is related to altering of composition due to evaporation of elements. The large amount of energy placed towards the center of the sample, resulting in the large area melt pool, could result in the evaporation of certain light elements such as N and Mn [49,50]. However, since these elements are austenite stabilizers, the formation of austenite at the center of the sample makes it clear that evaporation of elements is unlikely to have a significant impact on the resulting phase formations in the build.

### 4.2. Correlation between solidification maps and processing conditions

Solidification maps provide useful information on the obtainable microstructures within a build based on the G and $V_s$ at the time of solidification. For steels, these maps give perspective ranges towards planar and dendritic $\delta$-ferrite and austenite [10,32,51,52]. An understanding of the solidification map for 17–4 PH will bring better insight towards site-specific microstructure design through development of better knowledge of the possible phase formations and morphologies that could form under PBF-LB/M at the time of solidification. IRF routines need to be leveraged to create these solidification maps. Such routines have been used previously in PBF-LB/M to plot solidification maps to explain potential phase evolutions within stainless steels [32,51].

For the IRF routines, thermodynamic data was extracted from ThermoCalc. Initial Gibbs-Thomson coefficients, diffusion coefficients, lattice parameters, and interface kinetic coefficients were taken from [10,32,53,54]. A full table of parameters can be found in Table 5. The resulting solidification map with the accompanying G and $V_s$ values at the time of solidification are presented in Fig. 11. This map shows that the majority of G and $V_s$ are within the $\delta$-ferrite solidification mode. There are a few points that fall within the planar and dendritic austenite solidification modes, however, from SEM (Fig. 4) neither of these morphologies were identified. There are multiple potential explanations for these inconsistencies. Tourret et al. [55] for instance identified the stability of dendrites at velocities higher than the absolute stability limit through laser AM simulations under synchrotron X-ray imaging. It may also be that, given that some of these points correlate to regions of high solidification velocity and/or low thermal gradients, it is also possible that these regions were some of the last to solidify. If so, they may have likely been remelted upon scanning of the next layer and resolidified as dendritic $\delta$-ferrite.

**Table 5**
Fundamental parameters used as inputs into the KGT interface response function model.

| Parameter | Value | Unit |
|---|---|---|
| Interface kinetic coefficient, $\mu_{\alpha,\gamma}$ | 10.0 | m ($s^{-1}$ $K^{-1}$) |
| **$\gamma$ - Austenite** | | |
| Diffusion coefficient, $D_{i,\gamma}$ | $5 \times 10^{-9}$ | $m^2$ $s^{-1}$ |
| Gibbs-Thomson coefficient, $\Gamma_\gamma$ | $3.2 \times 10^{-6}$ | m K |
| Lattice coefficient, $a_{0,\gamma}$ | $3.6 \times 10^{-10}$ | M |
| **$\delta$ – Ferrite** | | |
| Diffusion coefficient, $D_{i,\delta}$ | $5 \times 10^{-8}$ | $m^2$ $s^{-1}$ |
| Gibbs-Thomson coefficient, $\Gamma_\delta$ | $2.6 \times 10^{-7}$ | m K |
| Lattice coefficient, $a_{0,\delta}$ | $2.9 \times 10^{-10}$ | M |

In consideration of changing processing parameters to encourage the austenite solidification mode, with the current 17–4 PH composition, it is deemed unlikely to observe any significant formation of dendritic austenite upon solidification based on the resulting solidification map shown in Fig. 11. As most PBF-LB/M processing parameters result in a spread of solidification velocities between $10^{-4}$ to $10^{0}$ and thermal gradients between $10^{4}$ to $10^{8}$ [52,56–60], it is unlikely to be able to manipulate the processing parameters to encourage the formation of dendritic austenite. Instead, adjustment of the composition through decreasing of the $Cr_{eq}/Ni_{eq}$ ratio would be necessary to potentially allow for some control of the solidification mode.

### 4.3. Formation and morphology of austenite

When studying the austenite formed throughout the build, a few noticeable trends deserve to be discussed. First, the cut off between the center primarily austenite region and outer ferrite region is sudden, with the center austenite region having a radius of roughly 200 μm before reaching a 100 μm transition region where the amount of austenite decreases, before finally reaching the primarily ferritic outer region. Second, noticeable different morphologies of austenite have occurred in the outer and transition regions of the sample. These morphologies include allotriomorphic austenite that has primarily developed along the smaller $< 100 >$ // BD BCC grains that form rings around the sample, and Widmanstätten austenite that has primarily formed along larger grains perpendicular to the circle of smaller $< 100 >$ // BD BCC grains.

#### 4.3.1. Formation of austenite

The transformation from ferrite to austenite is traditionally considered a reconstructive process dependent on diffusional mechanisms. In consideration, high cooling rates and thermal gyrations have played a large role in influencing the formation of austenite observed here. The 1D concentration plots in Fig. 6c are prime indicators on the impact of solidification and diffusion. Here, the 1D concentration plots for the solute elements show steep concentration gradients at the interface known as diffusion spikes that are only a few nanometers in length. These short diffusion spikes occur under high undercooling where solute elements cannot diffuse fast enough upon solidification of the melt pool [61]. Therefore, the APT results indicate that only very limited diffusion has occurred for the solute elements between the austenite and ferrite.

Therefore, the transformation of ferrite to austenite is dependent on fast diffusing interstitial elements such as C and N, which are potent austenite stabilizers. These elements can readily diffuse during solidification and periods of elevated temperatures that occur through the thermal gyrations imposed by the layer-by-layer process of PBF-LB/M. Within literature, cooling rate analyses done under welding conditions help point towards N and C being the main limiting factors towards austenite formation. Here, their experiments showed that despite minimal diffusion of elements such as Cr and Ni, if cooling rates were of such magnitudes to permit diffusion of N and C within the welds, the nucleation and growth of austenite could occur [62–65].

Other elements were noted to lack any substantial diffusion under these experiments due to their slower diffusion rates coupled with the relatively fast cooling rates, such that only limited partitioning occurred for solute elements such as Cr, Si, Cu, Mo, and Ni. While the composition differences between the two phases for Cr and Si specifically are low, (< 1 at%) it is interesting that these ferrite stabilizers partitioned more to the austenite phase. Under PBF-LB/M of 17–4 PH, the fast cooling rates result in fine heterogenous microstructures (i.e. dendrites) that have

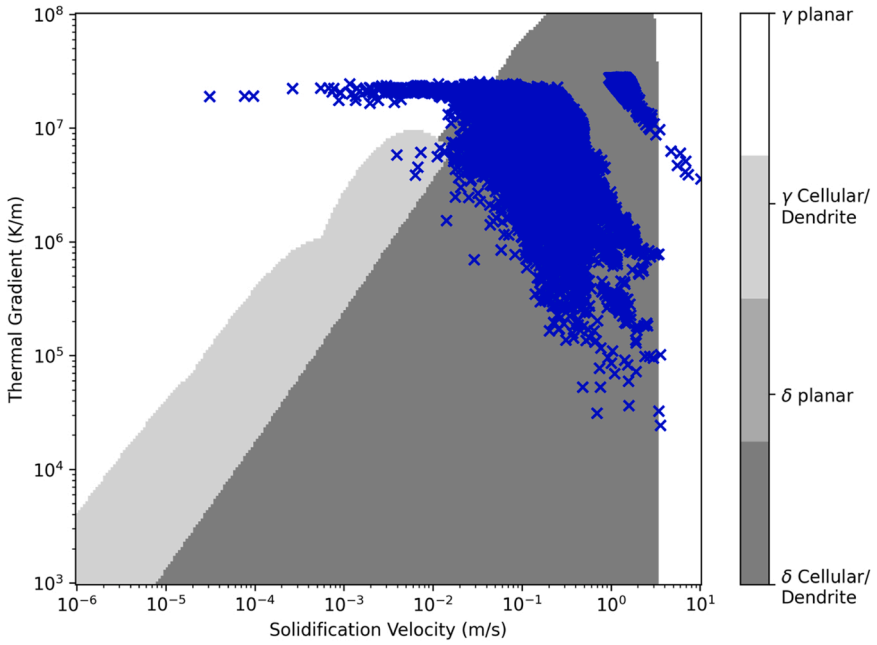


**Fig. 11.** Predicted phase map for 17–4 PH based on the thermal gradients and solidification velocity at the time of solidification of the melt pool. Blue ×s represent the thermal gradients and solidification velocity predicted by OpenFOAM for the concentric scan strategy.

short diffusion lengths, with reported dendrite sizes of only a couple of microns in alloy steels printed via PBF-LB/M [66,67]. It is thus likely that these discontinuities in elemental partitioning between phases in the build must have been impacted by these heterogeneities that are too large to be directly observable through APT. It is likely, as mentioned previously, that N and C have diffused and assisted nucleation of austenite, but the thermal conditions experienced have not enabled solute elements such as Cr, Si, Mo, and Ni to diffuse significantly and the individual phases to reach an equilibrium state.

Due to the noticeable contrast between the inner austenite and outer ferrite regions, relations can be made through analysis of thermal history at select locations. Fig. 12 shows temperature versus time plots for the last solidification event of select "temperature probe" locations and the next proceeding 3rd, 5th, and 7th layers. The exact locations are taken where y equals 5 mm, z equals 0 mm, and x equals 4.7, 4.8, 4.9, and 5.0 mm on the XY plane of the thermal simulation. The temperature

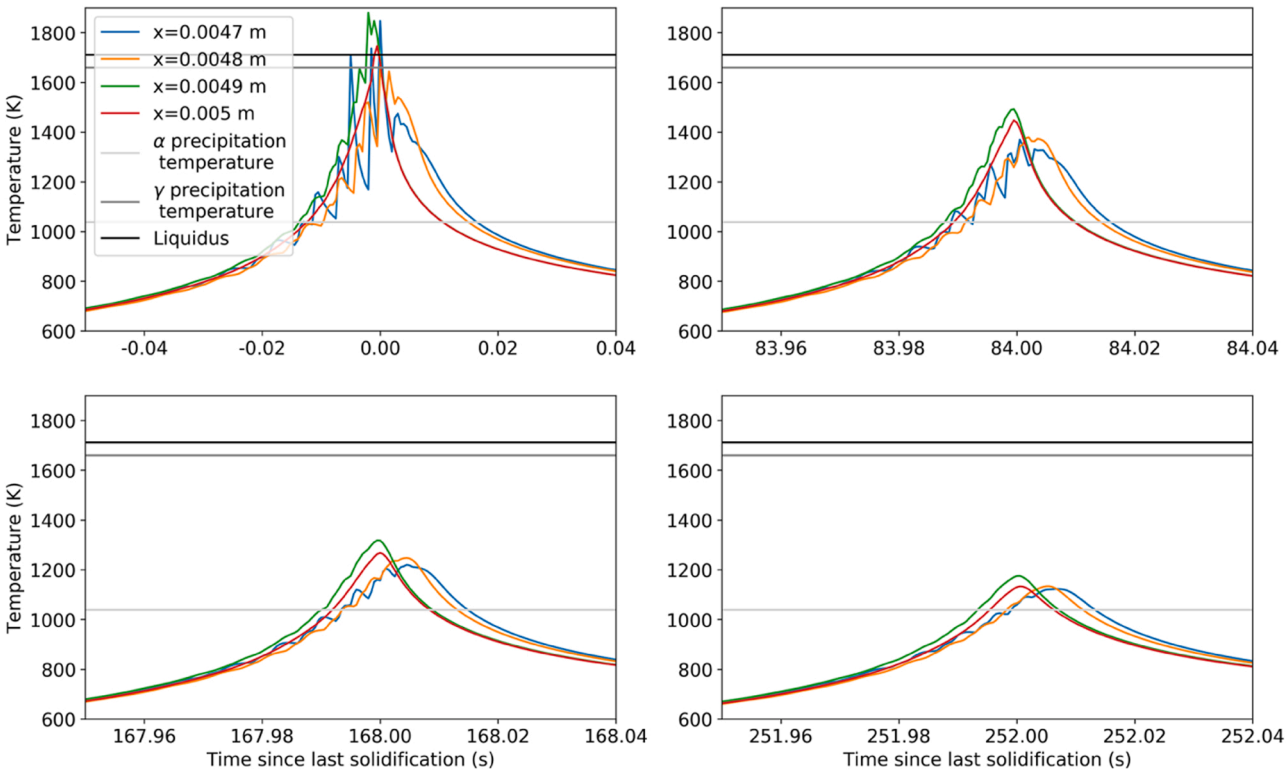


**Fig. 12.** Temperature versus time after last solidification and the proceeding 3rd, 5th, and 7th layers.

probes at 4.7 and 4.8 mm roughly coincide with the outer ferrite region and/or transition region. The probe at 4.9 mm coincides with the inner ring of austenite. The temperature probe at 5.0 mm coincides within the inner region of BCC. Time at 0 s correlates to the last point the temperature is above the solidus temperature.

The temperature probes at 4.7, 4.8 and 4.9 mm all show fluctuations leading up to their peak temperature. These fluctuations are linked to the concentric scan strategy which heats up the surrounding regions as the laser passes nearby. Temperature probes at 4.7 and 4.8 mm see larger fluctuations in temperature compared to the probe at 4.9 mm as there is more time between each pass of the laser. Thus, the regions at the temperature probe at 4.7 and 4.8 mm cool more before another laser pass occurs. Comparatively, the temperature probe at 5.0 mm sees no fluctuations in part due to the formation of an area melt pool. This melt pool disappears only once the laser is turned off and thus the region close to the center of the sample experiences significantly fewer thermal gyrations compared to the other temperature probes. Further interesting observations include the generally slower cooling rates, after solidification, for temperature probes 4.7 and 4.8 mm during the first layer and the trend for the temperature probe at 4.9 mm to consistently having the highest peak temperature for every layer when compared to all other temperature probes.

From these observations, no one trend can be identified as the primary cause for the formation of the inner austenite ring. However, a combination of factors needs to be considered, including the thermal gyrations (i.e., temperature fluctuations), the peak temperature experienced in each layer, and the cooling rate at each probe. Overall, these results highlight the complex link between thermal history and the resulting phase response. Further work is required to identify the links between thermal history and the nucleation and growth of austenite.

#### 4.3.2. Grain structure and cooling rate influences on austenite morphology

The site-specific formation of different morphologies of austenite can largely be explained through differences in grain size and cooling conditions. The allotriomorphic austenite is more likely to form in regions with a higher density of $\delta/\delta$ grain boundaries that serve as nucleation points for austenite [68]. Therefore, allotriomorphic austenite is primarily found around the smaller $< 100 >$ // BD BCC grains that solidified at the center of the melt pool track. In general, the higher number of nucleation points increases the likelihood of allotriomorphic austenite forming while preventing the formation of Widmanstätten austenite.

Widmanstätten austenite precipitates at high cooling rates and in regions where allotriomorphic austenite is absent [69]. Therefore, Widmanstätten austenite can be found primarily along the $\delta/\delta$ grain boundaries of larger grains perpendicular to the group of smaller $< 100 >$ // BD line of grains that formed at the center of the melt pool track as seen in Fig. 3a. Fig. 3c also confirms the growth of austenite with this morphology depending on the thermal gyrations experienced by the phases. Here, allotriomorphic and Widmanstätten austenite have grown due to the continued diffusion of certain elements (e.g., C and N) and slower cooling conditions towards the center of the sample.

### 4.4. Transformation of austenite to ferrite and/or martensite

From Fig. 4c, it is clear that towards the center of the sample, some BCC microstructures precipitated through a solid-state transformation from the austenite. This is identified through the lack of any solidification features (i.e., dendrites). Single banded BCC microstructures can be seen within individual austenite grains and collections of BCC lath structures (indicated by white arrows) are also present. These BCC structures were only noted towards the center of the sample in the heavily austenite region. Unfortunately, due to the possibility of transforming austenite to martensite during the necessary polishing routine, it cannot be directly said as to whether these phases, that transformed within the austenite grains, formed during the PBF-LB/M process or were induced during the polishing step. However, it should be noted that the single individual bands of BCC identified within austenite grains is unique for PBF-LB/M 17–4 PH, and to the best knowledge of the authors has not been identified previously. Thus, in this section, we discuss the identified single banded BCC phase, the limited formation of a lath BCC microstructure, and the possible reasons for the stability of austenite within the build and its lack of transformation to martensite.

Based on morphology, the individual bands of BCC may be $\alpha$-ferrite. As the majority of the equilibrium phase shown in Fig. 10 up to ~900 K (627 ℃) is mostly $\alpha$-ferrite, there is an opportunity that at the center of the sample some amount of $\alpha$-ferrite could have precipitated, due to slower cooling rates and longer times spent at these elevated temperatures. The exact identity of these banded BCC microstructures was not identified here. Future work through either site-specific transmission electron microscopy or APT could be used to identify this BCC structure, but this is beyond the scope of this study.

The large cluster of BCC laths in Fig. 4b-c (pointed to by white arrows) towards the center of the sample could be martensite, however, many factors make confirmation of martensite formation and its identification within these samples difficult. What is clear however is that the formation of this lath BCC phase was limited. The phase transformation from austenite to martensite is a displacive mechanism and occurs upon fast cooling below the martensite start ($M_s$) temperature. For 17–4 PH processed through traditional methods, martensite formation is common, however, under PBF-LB/M, reports on the formation of martensite and its phase fraction vary [6,8,15,43,70]. Multiple factors can influence martensite formation and suppress its formation including composition, grain size, dislocation content, and the stress/strain state [11].

Considering grain size, its effect on the $M_s$ temperature is rooted in the increase in work necessary to plastically deform the lattice due to increases in the yield stress as explained through the Hall-Petch relationship [70]. With decreasing grain size, the yield stress increases, and, in turn, more work is necessary to plastically deform the lattice during the transformation of austenite to martensite. For austenite in the concentric sample, the grain size was noted to average around 3 μm. In literature, many studies report that grain sizes of ~10 μm or less had an appreciable impact on the $M_s$ temperature for various alloys [71–73].

A second consideration is the local composition. In general, solute alloying elements within 17–4 PH can suppress the $M_s$ temperature depending on how they segregate [74,75]. PBF-LB/M samples see large heterogeneities in the microstructure with solute rich interdendritic regions. Other work has demonstrated the suppression of martensite formation in a tool steel showing it is possible to stabilize austenite due to segregation within PBF-LB/M samples [76]. From the APT data (Fig. 6), the austenite sees a compositional makeup that is heavily enriched in solute and interstitial elements leaving a $M_s$ temperature below room temperature as a possibility.

The impact that the grain size and composition can have on the $M_s$ temperature can be calculated with ThermoCalc. If assuming a grain size of 3 μm and the base powder composition, then the calculated $M_s$ temperature is 347 K (74 ℃). This $M_s$ temperature would then indicate some transformation of austenite to martensite at room temperature. If we consider local composition (from APT), with the assumption that 0.11 wt% N, based on the idea that four-fifths of all N segregated to austenite based on the NbN results, then the $M_s$ temperature drops to 228 K (−45 ℃). The significant drop in the $M_s$ temperature can be attributed to local increases in the solute including increases in Ni (from 4.06 to 8.85 at%), Si (from 1.39 to 1.88 at%), estimated N content (0.39–0.45 at%), and a decrease in Fe content (from 72.6 to 69.5 at%). It should be noted that APT is a highly localized technique and does not necessarily represent the entire sample, especially when considering the microstructure heterogeneities found within the PBF-LB/M process. EPMA results in Fig. 5 demonstrate how on the μm scale these compositional variations may not be evident. Therefore, while the $M_s$ temperature is below room temperature for the region of interest for APT, other regions such as possibly seen in Fig. 4 may not necessarily have

local compositions where the martensite temperature is below room temperature.

Stress can also play a role in assisting or suppressing the formation of martensite. Due to the high amount of stress present in PBF-LB/M, samples stress is worth discussing here [77,78]. Stress primarily interacts with the shape deformation of martensite and assists similar to thermally activated martensite. Therefore, stress can contribute or suppress the driving force for the nucleation of martensite. Patel and Cohen [79] outlined the impact of stress on the $M_s$ temperature noting that uniaxial compressive stresses and tensile stresses increased the $M_s$ temperature while hydrostatic stresses were known to decrease the $M_s$ temperature. Through the use of neutron diffraction at ANSTO and the KOWARI strain scanner [80], it was found that the sample in this work had large amounts of compressive stresses at the center of the sample. The full result of this work is presented in the Supplementary File (Section S1 and Supplementary Fig. S1). However, in short, due to difficulties in obtaining a stress free $d_0$ value, information on the micro-stresses caused by mismatch of the elastic, plastic, and thermal properties is unknown. Only the macro-stresses which represent the residual stress could be reconstructed from the neutron diffraction data. These macro-stresses were reconstructed assuming constant $d_0$ for both phases and assuming force balance conditions and stress boundary conditions for the appropriate stress components. Thus, an exact statement on the impact of stress on the martensite formation on these samples cannot be made outright due to the lack of information on how micro-stresses could be interacting with the local microstructure. It is recommended, regardless, that due to the high amounts of residual stress present in these samples (up to 1404 MPa), consideration should be made in the future involving the impact that stresses might be having on the formation of martensite in steels due to the PBF-LB/M process.

### 4.5. Significance of findings

Through the experimental and computational analyses performed here, a summary of the potential phase evolution is presented in a flow chart in Fig. 13. In short, it is concluded that the entire build solidifies as $\delta$-ferrite. Depending on the cooling rate, $\delta$-ferrite may either remain present until room temperature or, if cooling rates are slower, transform into two morphologies of austenite. From there, the austenite can either remain stable until room temperature or yet again undergo a solid-state phase transformation to either to $\alpha$-ferrite or martensite. The formation of martensite due to grain size and local composition will be heavily suppressed, making the chances for this phase to form slim. However, it should not be fully disregarded as slight changes in 17–4 PH composition may result in higher martensite fractions at room temperature. For $\alpha$-ferrite, likely extended time at elevated temperatures is required for nucleation and growth.

## 5. Conclusion

The work presented here demonstrates the sensitivity of 17–4 PH to printing parameters. Through the use of a unique concentric scan strategy, site-specific evolution of microstructures (phases and their morphologies) occurred, where a predominantly austenitic microstructure formed at the center of the sample and a predominantly ferritic microstructure formed at the outer regions of the sample. These individual microstructural features are rationalized through a combination of experimental analysis and computational methods. These results demonstrate how 17–4 PH steel is highly sensitive to the thermal gyrations and cooling rates experienced within the PBF-LB/M process. The major findings can be summarized as follows:

- The build is identified to have an outer ferritic region and an inner austenite region. The difference in austenite and ferrite content between the inner and outer regions is linked to the progression of the concentric scan, resulting in a decrease in the cooling rate towards the center of the sample.
- The austenite is found to be solute rich, containing elements that are either austenite or ferrite stabilizers. Due to limited partitioning of the ferrite forming elements to ferrite, it is believed that diffusion of N and C is the rate limiting factor for the formation of austenite.
- Allotriomorphic and Widmanstätten austenite are identified. The allotriomorphic austenite is noted to form primarily along the smaller $< 100 >$ // BD BCC grains parallel to the build direction that formed in the center of the melt pool tracks. Widmanstätten austenite forms along larger grains perpendicular to the smaller $< 100 >$ // BD line of BCC grains.
- BCC phases are found to have precipitated in the solid. BCC with a band structure is believed to be of $\alpha$-ferrite that had precipitated from the austenite. Clusters of BCC laths are identified as either ferrite or martensite. It is postulated that despite having an alloy composition that supports the formation of martensite, this phase transformation was most likely suppressed due to the compositional heterogeneity and austenite grain size in the sample.
- The phase evolution in the given 17–4 PH alloy used here for PBF-LB/M can be summarized as forming $\delta$-ferrite from the liquid. From there it can either transform to austenite or cool to room temperature and remain $\delta$-ferrite. Austenite can then either continue to grow or transform to either $\alpha$-ferrite or martensite, depending on the cooling rate. Therefore, due to the notable sensitivity of thermal signature with localized phase transformation, it can be concluded that microstructural engineering of phase is possible in PBF-LB/M.

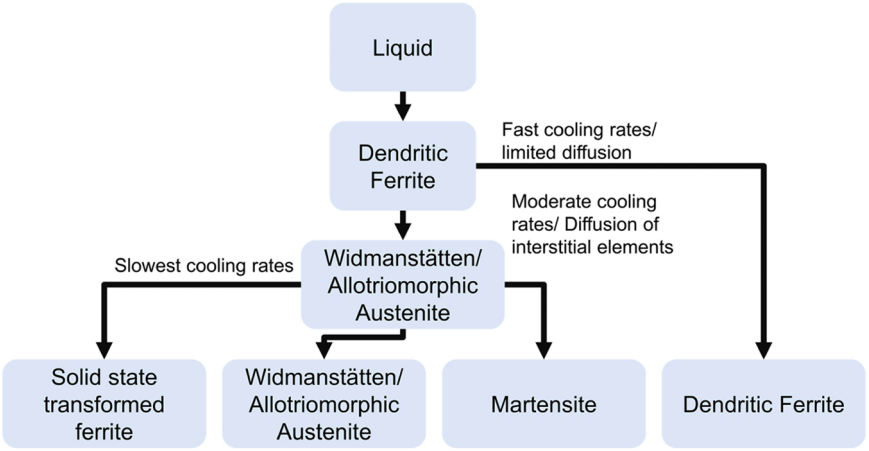


**Fig. 13.** Flow chart of identified phase transformations within the 17–4 PH samples printed using the concentric scan strategy.

This can be accomplished through site-specific manipulation of the scan strategy and processing parameters, to achieve specific thermal signatures that encourage the nucleation of the desired phase.

## CRediT authorship contribution statement

**Michael Haines:** Writing – review & editing, Writing – original draft, Visualization, Software, Investigation, Formal analysis, Conceptualization. **Moyle Maxwell:** Writing – review & editing, Methodology, Conceptualization. **Nima Haghdadi:** Writing – review & editing, Supervision, Project administration, Conceptualization. **Sophie Primig:** Writing – review & editing, Supervision, Project administration, Funding acquisition, Conceptualization. **Vitor Rielli:** Writing – review & editing, Visualization, Investigation, Formal analysis. **Vladimir Luzin:** Writing – review & editing, Investigation, Formal analysis.

## Declaration of Competing Interest

The authors declare that they have no known competing financial interests or personal relationships that could have appeared to influence the work reported in this paper.

## Data Availability

Data will be made available on request.

## Acknowledgements

Funding from the AUSMURI program administered by the Australia's Department of Industry, Science, Energy and Resources is acknowledged. The authors acknowledge the facilities, as well as the scientific and technical support of the Microscopy Australian node at the Electron Microscope Unit, UNSW Sydney (Mark Wainwright center) and Sydney Microscopy & Microanalysis (SMM) at the University of Sydney (a core research facility). The authors also thank Dr. Karen Privat at UNSW Sydney for her technical and scientific assistance. We would like also to acknowledge the Australian Nuclear Science and Technology Organization for provision of neutron beamtime at the KOWARI diffractometer through the user access program under proposal 9147.

## Appendix A. Supporting information

Supplementary data associated with this article can be found in the online version at doi:10.1016/j.addma.2023.103686.

## References

[1] A. Barz, T. Buer, H.D. Haasis, A study on the effects of additive manufacturing on the structure of supply networks, IFAC-Pap. 49 (2016) 72–77, https://doi.org/10.1016/j.ifacol.2016.03.013.
[2] S.S. Babu, N. Raghavan, J. Raplee, S.J. Foster, C. Frederick, M. Haines, R. Dinwiddie, M.K. Kirka, A. Plotkowski, Y. Lee, R.R. Dehoff, Additive manufacturing of nickel superalloys: opportunities for innovation and challenges related to qualification, Metall. Mater. Trans. A Phys. Metall. Mater. Sci. 49 (2018) 3764–3780, https://doi.org/10.1007/s11661-018-4702-4.
[3] M.M. Kirka, P. Nandwana, Y. Lee, R.R. Dehoff, Solidification and solid-state transformation sciences in metals additive manufacturing, Scr. Mater. 135 (2017) 130–134, https://doi.org/10.1016/j.scriptamat.2017.01.005.
[4] Z. Hu, S. Mahadevan, Uncertainty quantification and management in additive manufacturing: current status, needs, and opportunities, Int. J. Adv. Manuf. Technol. (2017) 1–20, https://doi.org/10.1007/s00170-017-0703-5.
[5] C.N. Hsiao, C.S. Chiou, J.R. Yang, Aging reactions in a 17-4 PH stainless steel, Mater. Chem. Phys. 74 (2002) 134–142, https://doi.org/10.1016/S0254-0584(01)00460-6.
[6] S. Vunnam, A. Saboo, C. Sudbrack, T.L. Starr, Effect of powder chemical composition on the as-built microstructure of 17-4 PH stainless steel processed by selective laser melting, Addit. Manuf. 30 (2019), 100876, https://doi.org/10.1016/j.addma.2019.100876.
[7] S.D. Meredith, J.S. Zuback, J.S. Keist, T.A. Palmer, Impact of composition on the heat treatment response of additively manufactured 17–4 PH grade stainless steel, Mater. Sci. Eng. A. 738 (2018) 44–56, https://doi.org/10.1016/j.msea.2018.09.066.
[8] Y. Sun, R.J. Hebert, M. Aindow, Effect of laser scan length on the microstructure of additively manufactured 17-4PH stainless steel thin-walled parts, Addit. Manuf. 35 (2020), 101302, https://doi.org/10.1016/j.addma.2020.101302.
[9] M.S. Moyle, N. Haghdadi, X.Z. Liao, S.P. Ringer, S. Primig, On the microstructure and texture evolution in 17-4 PH stainless steel during laser powder bed fusion: towards textural design, J. Mater. Sci. Technol. 117 (2022) 183–195, https://doi.org/10.1016/j.jmst.2021.12.015.
[10] S. Babu, J. Elmer, J. Vitek, S. David, Time-resolved X-ray diffraction investigation of primary weld solidification in Fe-C-Al-Mn steel welds, Acta Mater. 50 (2002) 4763–4781, https://doi.org/10.1016/S1359-6454(02)00317-8.
[11] S. Cheruvathur, E.A. Lass, C.E. Campbell, Additive manufacturing of 17-4 PH stainless steel: post-processing heat treatment to achieve uniform reproducible microstructure, Jom 68 (2016) 930–942, https://doi.org/10.1007/s11837-015-1754-4.
[12] M. Alnajjar, F. Christien, C. Bosch, K. Wolski, A comparative study of microstructure and hydrogen embrittlement of selective laser melted and wrought 17–4 PH stainless steel, Mater. Sci. Eng. A. 785 (2020), https://doi.org/10.1016/j.msea.2020.139363.
[13] M. Alnajjar, F. Christien, K. Wolski, C. Bosch, Evidence of austenite by-passing in a stainless steel obtained from laser melting additive manufacturing, Addit. Manuf. 25 (2019) 187–195, https://doi.org/10.1016/j.addma.2018.11.004.
[14] T. LeBrun, T. Nakamoto, K. Horikawa, H. Kobayashi, Effect of retained austenite on subsequent thermal processing and resultant mechanical properties of selective laser melted 17-4 PH stainless steel, Mater. Des. 81 (2015) 44–53, https://doi.org/10.1016/j.matdes.2015.05.026.
[15] H. Irrinki, S.D. Nath, M. Alhofors, J. Stitzel, O. Gulsoy, S.V. Atre, Microstructures, properties, and applications of laser sintered 17-4PH stainless steel, J. Am. Ceram. Soc. 102 (2019) 5679–5690, https://doi.org/10.1111/jace.16372.
[16] V.V. Rielli, F. Theska, S. Primig, Correlative approach for atom probe sample preparation of interfaces using plasma focused ion beam without lift-out, Microsc. Micro 28 (2022) 998–1008, https://doi.org/10.1017/S1431927621000349.
[17] J. Coleman, A. Plotkowski, B. Stump, N. Raghavan, A. Sabau, M. Krane, J. Heigel, D.R. Ricker, L. Levine, S. Babu, Sensitivity of thermal predictions to uncertain surface tension data in laser additive manufacturing, J. Heat. Transf. (2020), https://doi.org/10.1115/1.4047916.
[18] B. Stump, A. Plotkowski, J. Coleman, Solidification dynamics in metal additive manufacturing: analysis of model assumptions, Model. Simul. Mater. Sci. Eng. 29 (2021), https://doi.org/10.1088/1361-651X/abca19.
[19] J. Goldak, A. Chakravarti, M. Bibby, A new finite element model for welding heat sources, Metall. Trans. B. 15 (1984) 299–305, https://doi.org/10.1007/BF02667333.
[20] A.S. Sabau, W.D. Porter, Alloy shrinkage factors for the investment casting of 17-4PH stainless steel parts, Metall. Mater. Trans. B Process. Metall. Mater. Process. Sci. 39 (2008) 317–330, https://doi.org/10.1007/s11663-007-9125-3.
[21] B. Cheng, S. Price, J. Lydon, K. Cooper, K. Chou, On Process Temperature in Powder-Bed Electron Beam Additive Manufacturing: Model Development and Validation, in: J. Manuf. Sci. Eng. Trans, 136, ASME, 2014, pp. 1–12, https://doi.org/10.1115/1.4028484.
[22] B. Cheng, S. Shrestha, K. Chou, Stress and deformation evaluations of scanning strategy effect in selective laser melting, Addit. Manuf. 12 (2016) 240–251, https://doi.org/10.1016/j.addma.2016.05.007.
[23] W. Kurz, B. Giovanola, R. Trivedi, Theory of microstructural development during rapid solidification, Acta Met. 34 (1986) 823–830.
[24] S. Fukumoto, W. Kurz, Solidification phase and microstructure selection maps for Fe-Cr-Ni alloys, ISIJ Int 39 (1999) 1270–1279, https://doi.org/10.2355/isijinternational.39.1270.
[25] M. Haines, A. Plotkowski, C.L. Frederick, E.J. Schwalbach, S.S. Babu, A sensitivity analysis of the columnar-to-equiaxed transition for Ni-based superalloys in electron beam additive manufacturing, Comput. Mater. Sci. 155 (2018) 340–349, https://doi.org/10.1016/j.commatsci.2018.08.064.
[26] S.A David, J.M. Vitek, Correlation between solidification parameters and weld microstructures, Int. Mater. Rev. 34 (1989) 213–245, https://doi.org/10.1179/imr.1989.34.1.213.
[27] O. Gokcekaya, T. Ishimoto, S. Hibino, J. Yasutomi, T. Narushima, T. Nakano, Unique crystallographic texture formation in Inconel 718 by laser powder bed fusion and its effect on mechanical anisotropy, Acta Mater. 212 (2021), 116876, https://doi.org/10.1016/j.actamat.2021.116876.
[28] M. Laleh, A.E. Hughes, M.Y. Tan, G.S. Rohrer, S. Primig, N. Haghdadi, Grain boundary character distribution in an additively manufactured austenitic stainless steel, Scr. Mater. 192 (2021) 115–119, https://doi.org/10.1016/j.scriptamat.2020.10.018.
[29] K. Li, J. Zhan, T. Yang, A.C. To, S. Tan, Q. Tang, H. Cao, L.E. Murr, Homogenization timing effect on microstructure and precipitation strengthening of 17–4PH stainless steel fabricated by laser powder bed fusion, Addit. Manuf. 52 (2022), 102672, https://doi.org/10.1016/j.addma.2022.102672.
[30] K.M. Bertsch, G. Meric de Bellefon, B. Kuehl, D.J. Thoma, Origin of dislocation structures in an additively manufactured austenitic stainless steel 316L, Acta Mater. 199 (2020) 19–33, https://doi.org/10.1016/j.actamat.2020.07.063.
[31] N. Raghavan, S. Simunovic, R. Dehoff, A. Plotkowski, J. Turner, M. Kirka, S. Babu, Localized melt-scan strategy for site specific control of grain size and primary dendrite arm spacing in electron beam additive manufacturing, Acta Mater. 140 (2017) 375–387, https://doi.org/10.1016/j.actamat.2017.08.038.
[32] A.J. Godfrey, J. Simpson, D. Leonard, K. Sisco, R.R. Dehoff, S.S. Babu, Heterogeneity and solidification pathways in additively manufactured 316L stainless steels, Metall. Mater. Trans. A. 53 (2022) 3321–3340, https://doi.org/10.1007/s11661-022-06747-6.

[33] F. Yan, W. Xiong, E. Faierson, G.B. Olson, Characterization of nano-scale oxides in austenitic stainless steel processed by powder bed fusion, Scr. Mater. 155 (2018) 104–108, https://doi.org/10.1016/j.scriptamat.2018.06.011.
[34] M.S. Moyle, N. Haghdadi, W.J. Davids, X.Z. Liao, S.P. Ringer, S. Primig, Evidence of in-situ Cu clustering as a function of laser power during laser powder bed fusion of 17–4 PH stainless steel, Scr. Mater. 219 (2022), 114896, https://doi.org/10.1016/j.scriptamat.2022.114896.
[35] A.S. Murthy, J.E. Medvedeva, D. Isheim, S.L. Lekakh, V.L. Richards, D.C.Van Aken, Copper precipitation in cobalt-alloyed precipitation-hardened stainless steel, Scr. Mater. 66 (2012) 943–946, https://doi.org/10.1016/j.scriptamat.2012.02.039.
[36] Z. Wang, X. Fang, H. Li, W. Liu, Atom probe tomographic characterization of nanoscale Cu-rich precipitates in 17-4 precipitate hardened stainless steel tempered at different temperatures, Microsc. Microanal. 23 (2017) 340–349, https://doi.org/10.1017/S1431927616012629.
[37] Z. Wang, H. Li, Q. Shen, W. Liu, Z. Wang, Nano-precipitates evolution and their effects on mechanical properties of 17-4 precipitation-hardening stainless steel, Acta Mater. 156 (2018) 158–171, https://doi.org/10.1016/j.actamat.2018.06.031.
[38] N. Raghavan, R. Dehoff, S. Pannala, S. Simunovic, M.M. Kirka, J. Turner, N. Carlson, S.S. Babu, Numerical modeling of heat-transfer and the influence of process parameters on tailoring the grain morphology of IN718 in electron beam additive manufacturing, Acta Mater. 112 (2016) 303–314, https://doi.org/10.1016/j.actamat.2016.03.063.
[39] Y. Tian, D. McAllister, H. Colijn, M. Mills, D. Farson, M. Nordin, S. Babu, Rationalization of microstructure heterogeneity in INCONEL 718 builds made by the direct laser additive manufacturing process, Metall. Mater. Trans. A Phys. Metall. Mater. Sci. 45 (2014) 4470–4483, https://doi.org/10.1007/s11661-014-2370-6.
[40] F. Villaret, X. Boulnat, P. Aubry, J. Zollinger, D. Fabrègue, Y. de Carlan, Modelling of delta ferrite to austenite phase transformation kinetics in martensitic steels: application to rapid cooling in additive manufacturing, Materialia 18 (2021), 101157, https://doi.org/10.1016/j.mtla.2021.101157.
[41] J.W. Elmer, S.M. Allen, T.W. Eagar, Microstructural development during solidification of stainless steel alloys, Metall. Trans. A. 20 (1989) 2117–2131, https://doi.org/10.1007/BF02650298.
[42] T. Koseki, M.C. Flemings, Solidification of undercooled Fe-Cr-Ni alloys: part II. Microstructural evolution, Metall. Mater. Trans. A Phys. Metall. Mater. Sci. 27 (1996) 3226–3240, https://doi.org/10.1007/BF02663873.
[43] P. Leo, M. Cabibbo, A. Del Prete, S. Giganto, S. Martínez-Pellitero, J. Barreiro, Laser defocusing effect on the microstructure and defects of 17–4 ph parts additively manufactured by slm at a low energy input, Metals 11 (2021), https://doi.org/10.3390/met11040588.
[44] S. Yeon, J. Yoon, T.B. Kim, S.H. Lee, T. Jun, Y. Son, K. Choi, Normalizing effect of heat treatment processing on 17-4 PH stainless steel manufactured by powder bed fusion, Metals 12 (2022) 704, https://doi.org/10.3390/met12050704.
[45] S. Sabooni, A. Chabok, S.C. Feng, H. Blaauw, T.C. Pijper, H.J. Yang, Y.T. Pei, Laser powder bed fusion of 17–4 PH stainless steel: a comparative study on the effect of heat treatment on the microstructure evolution and mechanical properties, Addit. Manuf. 46 (2021), 102176, https://doi.org/10.1016/j.addma.2021.102176.
[46] T.J. Lienert, J.C. Lippold, Improved weldability diagram for pulsed laser welded austenitic stainless steels, Sci. Technol. Weld. Join. 8 (2003) 1–9, https://doi.org/10.1179/136217103225008847.
[47] L. Thijs, K. Kempen, J.P. Kruth, J. Van Humbeeck, Fine-structured aluminium products with controllable texture by selective laser melting of pre-alloyed AlSi10Mg powder, Acta Mater. 61 (2013) 1809–1819, https://doi.org/10.1016/j.actamat.2012.11.052.
[48] Y. Sun, R.J. Hebert, M. Aindow, Effect of heat treatments on microstructural evolution of additively manufactured and wrought 17-4PH stainless steel, Mater. Des. 156 (2018) 429–440, https://doi.org/10.1016/j.matdes.2018.07.015.
[49] A. Arabi-Hashemi, X. Maeder, R. Figi, C. Schreiner, S. Griffiths, C. Leinenbach, 3D magnetic patterning in additive manufacturing via site-specific in-situ alloy modification, Appl. Mater. Today 18 (2020), https://doi.org/10.1016/j.apmt.2019.100512.
[50] I. Ferretto, A. Borzi, D. Kim, N.M. della Ventura, E. Hosseini, W. Lee, C. Leinenbach, Control of microstructure and shape memory properties of a Fe-Mn-Si based shape memory alloy during Laser Powder Bed Fusion, SSRN Electron. J. 3 (2022), 100091, https://doi.org/10.2139/ssrn.4160455.
[51] D. Galicki, B.C. Chakoumakos, S.P. Ringer, M. Eizadjou, C.J. Rawn, K. Nomoto, S. S. Babu, On the formation of spherical metastable BCC single crystal spatter particles during laser powder bed fusion, Materialia 9 (2020), 100584, https://doi.org/10.1016/j.mtla.2020.100584.
[52] C. Hensley, K. Sisco, S. Beauchamp, A. Godfrey, H. Rezayat, T. McFalls, D. Galicki, F. List, K. Carver, C. Stover, D.W. Gandy, S.S. Babu, Qualification pathways for additively manufactured components for nuclear applications, J. Nucl. Mater. 548 (2021), 152846, https://doi.org/10.1016/j.jnucmat.2021.152846.
[53] S. Fukumoto, W. Kurz, Prediction of the.DELTA. to.GAMMA. Transition in austenitic stainless steels during laser treatment, ISIJ Int 38 (1998) 71–77, https://doi.org/10.2355/isijinternational.38.71.
[54] G. Jacob, Prediction of solidification phases in Cr-Ni stainless steel alloys manufactured by laser based powder bed fusion, Process, NIST Adv. Manuf. Ser. 100- 14 (2018) 1–38.
[55] D. Tourret, J. Klemm-Toole, A.E. Castellanos, B. Rodgers, G. Becker, A. Saville, B. Ellyson, C. Johnson, B. Milligan, J. Copley, R. Ochoa, A. Polonsky, K. Pusch, M. P. Haines, K. Fezzaa, T. Sun, K. Clarke, S. Babu, T. Pollock, A. Karma, A. Clarke, Morphological Stability of Solid-Liquid Interfaces Under Additive Manufacturing Conditions, Acta Mater. 250 (2023), 118858, https://doi.org/10.1016/j.actamat.2023.118858.
[56] P.W. Liu, Z. Wang, Y.H. Xiao, R.A. Lebensohn, Y.C. Liu, M.F. Horstemeyer, X. Y. Cui, L. Chen, Integration of phase-field model and crystal plasticity for the prediction of process-structure-property relation of additively manufactured metallic materials, Int. J. Plast. 128 (2020), 102670, https://doi.org/10.1016/j.ijplas.2020.102670.
[57] P. Liu, Z. Wang, Y. Xiao, M.F. Horstemeyer, X. Cui, L. Chen, Insight into the mechanisms of columnar to equiaxed grain transition during metallic additive manufacturing, Addit. Manuf. 26 (2019) 22–29, https://doi.org/10.1016/j.addma.2018.12.019.
[58] X. Li, W. Tan, Numerical investigation of effects of nucleation mechanisms on grain structure in metal additive manufacturing, Comput. Mater. Sci. 153 (2018) 159–169, https://doi.org/10.1016/j.commatsci.2018.06.019.
[59] M. Haines, F. List, K. Carver, D. Leonard, A. Plotkowski, C. Fancher, R. Dehoff, S. Babu, Role of scan strategies and heat treatment on grain structure evolution in Fe-Si soft magnetic alloys made by laser – powder bed fusion, Addit. Manuf. 50 (2021), 102578, https://doi.org/10.1016/j.addma.2021.102578.
[60] Y.S. Lee, W. Zhang, Modeling of heat transfer, fluid flow and solidification microstructure of nickel-base superalloy fabricated by laser powder bed fusion, Addit. Manuf. 12 (2016) 178–188, https://doi.org/10.1016/j.addma.2016.05.003.
[61] S.S. Babu, K. Hono, T. Sakurai, Atom probe field ion microscopy study of the partitioning of substitutional elements during tempering of a low-alloy steel martensite, Metall. Mater. Trans. A. 25 (1994) 499–508, https://doi.org/10.1007/BF02651591.
[62] T. Omura, T. Kushida, Y. Komizo, Nitrogen distribution on rapid solidification in laser welded duplex stainless steels, Weld. Int. 14 (2000) 288–294, https://doi.org/10.1080/09507110009549181.
[63] W. Zhang, T. DebRoy, T.A. Palmer, J.W. Elmer, Modeling of ferrite formation in a duplex stainless steel weld considering non-uniform starting microstructure, Acta Mater. 53 (2005) 4441–4453, https://doi.org/10.1016/j.actamat.2005.05.040.
[64] A.M. Meyer, M.Du Toit, Interstitial diffusion of carbon and nitrogen into heat-affected zones of 11-12% chromium steel welds, Weld. J. 80 (2001) 275–280.
[65] T. Ogawa, T. Koseki, Effect of composition profiles on metallurgy and corrosion behavior of duplex stainless-steel weld metals, Weld. J. 68 (1989) S181–S191.
[66] T. Mukherjee, H.L. Wei, A. De, T. DebRoy, Heat and fluid flow in additive manufacturing – part II: powder bed fusion of stainless steel, and titanium, nickel and aluminum base alloys, Comput. Mater. Sci. 150 (2018) 369–380, https://doi.org/10.1016/j.commatsci.2018.04.027.
[67] L. Cui, D. Deng, F. Jiang, R.L. Peng, T. Xin, R.T. Mousavian, Z. Yang, J. Moverare, Superior low cycle fatigue property from cell structures in additively manufactured 316L stainless steel, J. Mater. Sci. Technol. 111 (2022) 268–278, https://doi.org/10.1016/j.jmst.2021.10.006.
[68] D.A. Porter, K.E. Easterling, M.Y. Sherif, Phase Transformations in Metals and Alloys. Third, CRC Press, Boca Raton, 2009.
[69] J.W.A. Menezes, H. Abreu, S. Kundu, H.K.D.H. Bhadeshia, P.M. Kelly, Crystallography of Widmanstätten austenite in duplex stainless steel weld metal, Sci. Technol. Weld. Join. 14 (2009) 4–10, https://doi.org/10.1179/136217108×341166.
[70] H.K. Rafi, D. Pal, N. Patil, T.L. Starr, B.E. Stucker, Microstructure and mechanical behavior of 17-4 precipitation hardenable steel processed by selective laser melting, J. Mater. Eng. Perform. 23 (2014) 4421–4428, https://doi.org/10.1007/s11665-014-1226-y.
[71] S. Takaki, K. Fukunaga, J. Syarif, T. Tsuchiyama, Effect of grain refinement on thermal stability of metastable austenitic steel, Mater. Trans. 45 (2004) 2245–2251, https://doi.org/10.2320/matertrans.45.2245.
[72] R. Colaço, R. Vilar, Stabilisation of retained austenite in laser surface melted tool steels, Mater. Sci. Eng. A. 385 (2004) 123–127, https://doi.org/10.1016/j.msea.2004.06.069.
[73] H.S. Yang, H.K.D.H. Bhadeshia, Austenite grain size and the martensite-start temperature, Scr. Mater. 60 (2009) 493–495, https://doi.org/10.1016/j.scriptamat.2008.11.043.
[74] L. Samek, E. De Moor, J. Penning, B.C.De Cooman, Influence of alloying elements on the kinetics of strain-induced martensitic nucleation in low-alloy, multiphase high-strength steels, Metall. Mater. Trans. A Phys. Metall. Mater. Sci. 37 (2006) 109–124, https://doi.org/10.1007/s11661-006-0157-0.
[75] W. Wu, L.Y. Hwu, D.Y. Lin, J.L. Lee, Relationship between alloying elements and retained austenite in martensitic stainless steel welds, Scr. Mater. 42 (2000) 1071–1076, https://doi.org/10.1016/S1359-6462(00)00339-0.
[76] C.Y. Chou, N.H. Pettersson, A. Durga, F. Zhang, C. Oikonomou, A. Borgenstam, J. Odqvist, G. Lindwall, Influence of solidification structure on austenite to martensite transformation in additively manufactured hot-work tool steels, Acta Mater. 215 (2021), 117044, https://doi.org/10.1016/j.actamat.2021.117044.
[77] I. Yadroitsev, I. Yadroitsava, Evaluation of residual stress in stainless steel 316L and Ti6Al4V samples produced by selective laser melting, Virtual Phys. Prototyp. 10 (2015) 67–76, https://doi.org/10.1080/17452759.2015.1026045.
[78] Y. Lu, S. Wu, Y. Gan, T. Huang, C. Yang, L. Junjie, J. Lin, Study on the microstructure, mechanical property and residual stress of SLM Inconel-718 alloy manufactured by differing island scanning strategy, Opt. Laser Technol. 75 (2015) 197–206, https://doi.org/10.1016/j.optlastec.2015.07.009.
[79] J.R. Patel, M. Cohen, Criterion for the action of applied stress in the martensitic transformation, Acta Met. 1 (1953) 531–538, https://doi.org/10.1016/0001-6160(53)90083-2.
[80] O. Kirstein, V. Luzin, U. Garbe, The strain-scanning diffractometer kowari, Neutron N. 20 (2009) 34–36.